The effects of space holder size and volume fraction on the geometric characteristics and performance of absorbable iron scaffolds

MSc Thesis

S. de Vries

Technische Universiteit Delft

The effects of space holder size and volume fraction on the geometric characteristics and performance of absorbable iron scaffolds

by

S. de Vries

in partial fulfilment of the requirements for the degree of

Master of Science
in Biomedical Engineering

at the Delft University of Technology,
to be defended publicly on Monday June 24, 2019 at 10:00 AM.

Student number: 4049608
Thesis committee: Dr. J. Zhou supervisor
Dr. Y. Gonzalez Garcia
Dr. ir. M. J. M. Hermans

TU Delft Delft University of Technology

Abstract

Background The number of orthopedic reconstruction procedures increases annually and the usage of autogenous bone grafts, although still being the gold standard for the treatment of bone defects, can cause donor site morbidity, pain, prolonged hospitalization and has a risk of deep infection. Another option is using an iron bone graft substitute, also called absorbable scaffold. Although many studies have been performed on porous absorbable iron scaffolds created by the space holder method, no studies have considered the influence of variations in space holders on absorbable scaffolds. The present study aimed to clarify the effects of space holder particle size and volume fraction, on the pore structure, resultant mechanical properties and absorbability of iron scaffolds.

Methods Spherical iron particles (D_{50}=40.16 μm) were used as the matrix powder and mixed with coarse (D_{50}=408.5 μm) and fine (D_{50}=248.6 μm) rectangular urea space holding particles in volume fractions of 20, 40 and 60%, to create six different scaffolds with the space holder method. Scanning electron microscopy (SEM) and energy-dispersive X-ray spectroscopy were used to observe the scaffolds surface. Thereafter x-ray microtomography (μCT) and Archimedes' tests were used to characterize the scaffolds topology. The absorbability of scaffolds was characterized by potentiodynamic polarization (PDP) measurements and weight loss measurements after 3 and 11 of days immersion in modified simulated body fluid (m-SBF). Mechanical properties were determined by performing diametral compression of the scaffolds, both before and after immersion in m-SBF.

Results SEM images showed that morphology of the final pores was similar to that of space holder particles. Pores at lower porosities are isolated and become more connective or fully connected at higher porosities. Archimedes' data showed that space holder fraction was directly related to porosity. Pore connectivity, measured by μCT, is higher for fine space holding particles. Until at 60% space holder volume fraction, the high amount of space holder particles agglomerated. Furthermore, it was observed that space holding particles had a large preference to move in a plane perpendicular to the applied compaction pressure. Diametral compression showed that increasing porosity resulted in lower yield strength and elastic modulus of scaffolds. The effects of space holder particle size and immersion time on mechanical properties were less pronounced. PDP measurements showed that the corrosion mechanism of scaffolds did not change due to change in space holder particle size or volume fraction. Weight loss measurements after 3 and 11 day immersion in m-SBF showed that increasing porosity resulted in higher weight loss of scaffolds. Weight loss was marginally affected by space holder particle size.

Conclusion Space holder particle size affected the created pore size and surface area yet also changed the pore connectivity. Similarly, the space holder volume fraction affected the created porosity and pore connectivity yet also changed the pore size and shape. This means that the pore structure not independently changes due to space holder particle size or fraction, but rather as a combination of both. Furthermore, in this study it was mainly the created porosity that influenced the mechanical properties and absorption rate of the scaffold. Space holder particle size did not show the same differentiating results, although this might be caused by agglomerating space holder particles and its dependency on volume fraction. Differentiating the created pore structure more and using a longer immersion time should be the next objectives in the determination of the effect of space holder particles on the performance of absorbable iron scaffolds for orthopedic applications.

Contents

1 Introduction

The number of orthopedic reconstruction procedures increases annually [1] and such procedures are performed in case of tumors, traumas, bone degeneration and diseases. In 2017 over 2.2 million bone graft transfers, at a total cost of approximately 2.5 billion dollars, were performed worldwide [2]. Most of these grafts are autogenous bone grafts, the gold standard for the treatment of bone defects. However, autogenous bone grafts can cause donor site morbidity, pain, prolonged hospitalization and have increased risk of deep infection and the availability of autogenous bone grafts is limited [3]. Another option is using a synthetic bone graft substitute, also called scaffold. Scaffolds can be made of metallic, ceramic, polymer or composite materials [4]. Until today, metals have shown the greatest potential as load-bearing orthopedic implants [5], owing to their excellent mechanical strength and resilience.

A majority of metallic implants have been made from bio-inert materials as titanium- based alloys, stainless steel, tantalum and cobalt-based alloys [4, 7, 8]. However permanent implants have disadvantages, such as prolonged physical irritation and chronic inflammation, which leads to implant failure [9]. Removing the implant in a second operation leads to a second defect at the implantation site, pain and increased treatment costs [10]. Biodegradability, or according to the new ASTM F3160-16 standard "absorbability", is therefore considered to be an important requirement for an ideal bone scaffold. Interest in these absorbable metals has been growing rapidly [11]. Absorbable metals are expected to corrode gradually *in vivo* by generating an appropriate host response and dissolve completely upon fulfilling the mission to assist tissue healing [6, 12]. The absorbable metal family includes iron, magnesium, zinc, and their alloys [4, 11]. All elements that can be found in the human body, the daily allowance and effects of an overdose of those elements can be found in Table 1.1. Since magnesium is a relatively non-toxic element with mechanical behavior similar to human bone, majority of the research has been dedicated

Table 1.1: Amount and effect of Mg, Fe and Zn in the human body [6]

Element	**Human amount (g)**	**Function**	**Toxicity**	**Daily allow. (mg)**
Mg	25	Activator of many enzymes; co-regulator of protein synthesis and muscle contraction; stabilizer of DNA and RNA	Excessive Mg leads to nausea	700
Fe	4-5	Component of several metalloproteins; crucial in vital biochemical activities, i.e. oxygen sensing and transport	Iron toxicity gives rise to lesions in the gastrointestinal tract, shock and liver damage	10-20
Zn	2	Trace element; appears in all enzyme classes; most Zn appears in muscle	Neurotoxic and hinder bone development at higher concentration	15

Table 1.2: Direct comparison in corrosion rate between pure Mg, Fe and Zn after 168h of immersion in Saline solution at 37°C [18]

Element	corrosion rate (mm/yr)
Mg	4
Fe	0.2
Zn	0.6

to magnesium-based scaffolds [13, 14]. The limitations of magnesium-based scaffolds are their high corrosion rate and the fact that magnesium corrosion is linked to hydrogen evolution [15–17]. Lowering the magnesium corrosion process can be done by alloying or coating, however, achieving appropriate time for new tissue growth is still a challenge [4, 11]. Therefore, current research is also focusing on more slowly corroding zinc and iron. A lack of standardization for determining corrosion rate makes comparisons difficult but Vojtěch et al. [18] created a direct comparison between absorbable metals, as can be seen in Table 1.2. This shows the large differences in corrosion rate between magnesium and the other absorbable metals. Zinc is said to have an optimal corrosion rate and its mechanical properties are close to that of magnesium, but *in vivo* research is still in early stage [19, 20]. Therefore, it will take a while before this new material can be used in scaffolds. Iron on the other hand is a plentiful element in the human body and is necessary for good functionality of many enzymes and oxygen transportation [21]. *In vivo* tests of bio-compatibility have been performed in several studies and all of them have shown that iron is a suitable material for absorbable load-bearing implants [22–25]. On the contrary, major disadvantage of iron-based scaffolds is its slow corrosion rate, as can be seen in Table 1.2, which must be enhanced for use in absorbable implantology [4, 11]. Furthermore, iron possesses significantly higher values of mechanical properties than zinc and magnesium, see Table 1.3. Mainly high stiffness can cause problems in the form of stress shielding, if implanted as a load-bearing scaffold [5, 26]. To prevent stress shielding, the stiffness of iron scaffolds should be decreased and in order to get a good corrosion rate in the human body, corrosion rate of iron scaffolds should be increased [4]. Both lowering mechanical properties and increasing the corrosion rate can be fulfilled by creating a porous implant with a larger surface area [13]. Hermawan et al. [11] mentioned in their review that iron seems to provide an optimum compromise of mechanical properties and corrosion behavior if used with fine 3D structures in a porous form. A porous form also benefits migration and proliferation of cells and allows mass transfer of nutrients, oxygen and waste metabolic products [4, 12].

An optimal porous design for orthopedic scaffolds is said to have macro pore size of approximately 100 to 400 μm, micro pore size $<$20 μm and an open, interconnected structure [27–30]. Since pore design is so important, the fabrication method to create pores becomes equally important. Various powder metallurgy techniques have been used to create a large variety of porous scaffolds, of which foaming, additive manufacturing and the space holder method have proven to be the most popular ones [24, 31–35]. Additive manufacturing is one of the most precise methods and allows for the fabrication of products that have very complex shapes and structures. However, this method is very expensive [5]. Foaming iron-based scaffolds is very difficult due to high density, high melting point, high surface tension and low viscosity of iron melt [21]. The space holder method (SHM) however, provides a lot of freedom since pore size and shape can easily be tuned by altering space holder particles and thereby influencing the type of porosity. In addition, it is a cheaper technique than additive manufacturing and capable of varying the porous design more easily than foaming.

Scaffold fabrication with SHM relies on temporary particles added to a metallic matrix powder, i.e., space holding particles that act as a pore former [36]. Space holding particles are, firstly, mixed and uniaxial compacted together with metallic matrix powder particles, resulting in the green compact, see

Table 1.3: Mechanical properties of absorbable metals as found in CES EduPack 2017

	Young's modulus (GPa)	Yield strength (MPa)
Iron	204 - 212	110 - 165
Zinc	90 - 110	80 - 160
Magnesium	44 - 45.5	65 - 100

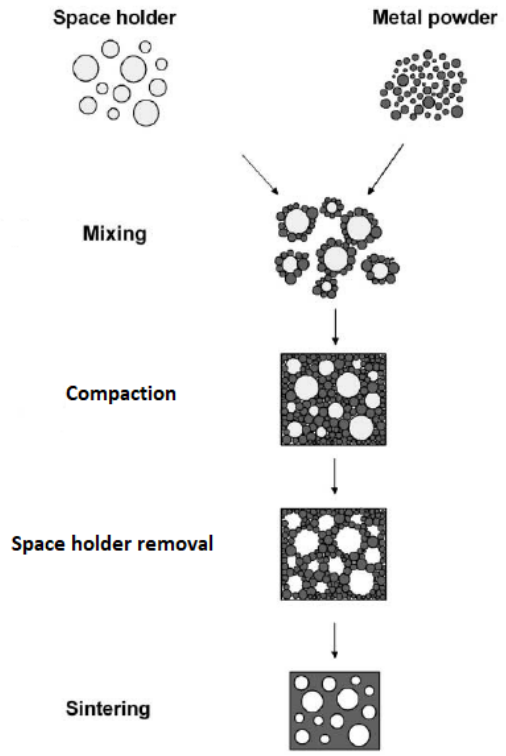

Figure 1.1: Space holder technique for making porous metallic structures from metal powders [37]

Figure 1.1. After compaction, the space holding particles are removed leaving new pores in the matrix of metallic powder particles. Lastly, the scaffold preform is sintered to create the final scaffold product.

Although many studies have been performed on porous absorbable iron scaffolds prepared using SHM, no studies have considered the influence of variations in space holders, despite the importance of the subject. The present study aims to clarify the effect of space holder particle size and volume fraction on the pore structure, resultant mechanical properties and absorbability of iron scaffolds. Two particle sizes and three volume fractions of space holders were used to design six different scaffolds. Surface, topological, corrosion and mechanical measurements were carried out to characterize these scaffolds.

2

Materials and Methods

2.1. Study outline

The outline of the study is presented in Figure 2.1.

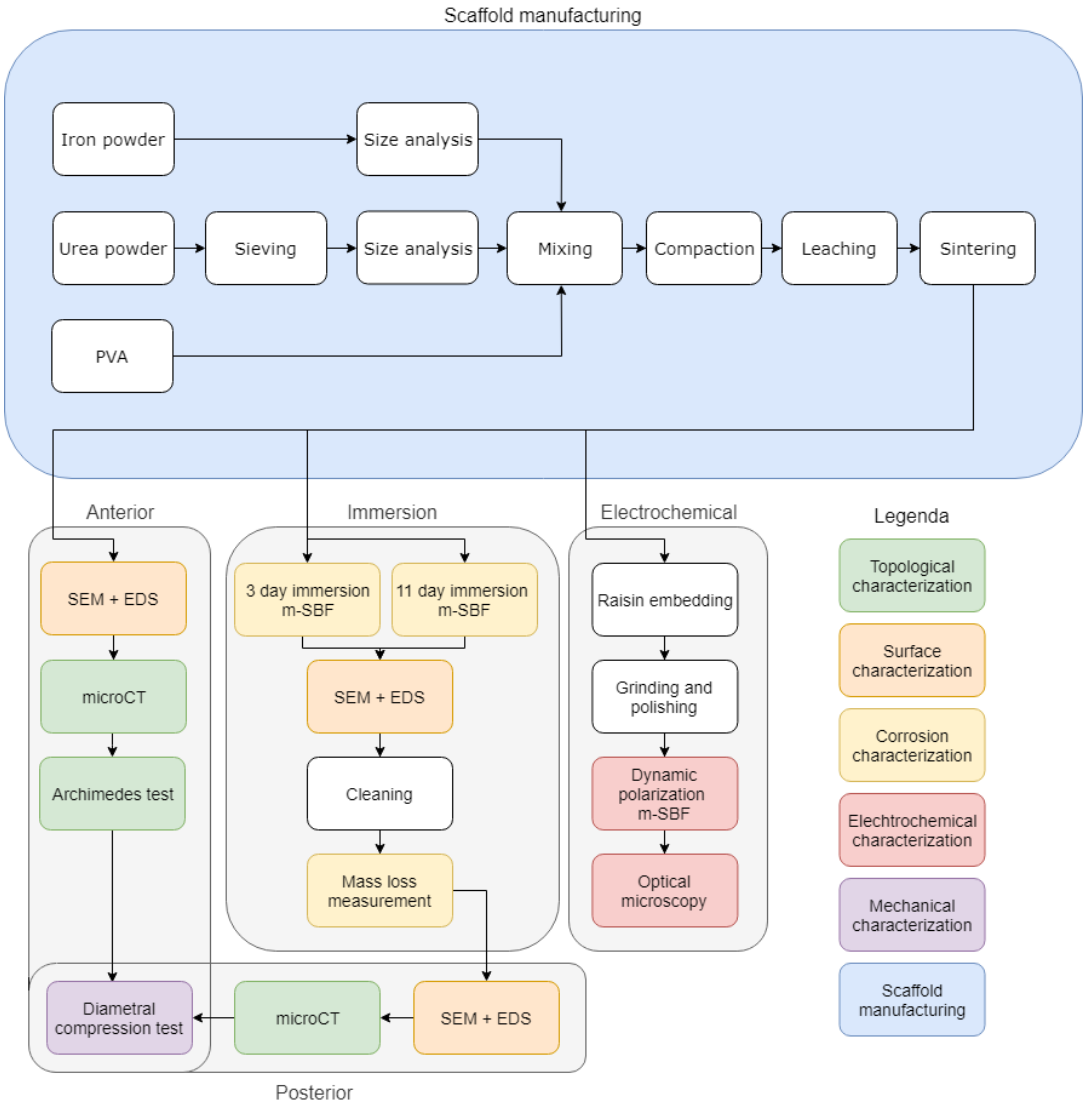

Figure 2.1: Schematic representation of study design

2.2. Scaffold manufacturing

This section contains information about how the scaffolds were manufactured, why scaffolds were manufactured this way and more background information about fabrication can be found in Appendix A.

2.2.1. Materials

Iron The metallic matrix powder was composed of nitrogen gas atomized Fe powder (Material Technology Innovations Co., China) with a purity of 99.88 wt.%. Particle size was D_{50}=40.16 μm with a spherical shape, see Figure 2.2a.

Urea The space holding particles were composed of rectangular carbamide (urea) powder of pharmaceutical grade (purity ≥ 99%), both in a large variant (Merck, Germany) (D_{50}=399.23 μm), see Figure 2.2b, and a small variant (GERBU Biotechnik GmbH, Germany) (D_{50}=296.79 μm), see Figure 2.2c. In order to create a larger and clearer difference between the two pore formers, both were sieved using a Haver EML digital plus siever (Haver & Boecker, Germany) for 30 minutes with an interval of 10 seconds at an amplitude of 0.3. The large variant powder was collected between sieves of 250 - 500 μm, hereafter called coarse urea, and the small variant was collected between sieves of 63 - 250 μm, hereafter called fine urea.

Particle sizes of both fine and coarse urea were analyzed using a Microtrac S3500 sizer (Microtrac, USA). The diameters of fine and coarse urea were determined to be D_{50}=248.6 μm and D_{50}=408.5 μm, respectively.

Polyvinyl alcohol Binder was prepared from polyvinyl-alcohol (PVA) powder (Alfa Aesar GmbH & Co KG, Germany) dissolved in demineralized water at 85°C, after which it was cooled down to room temperature. A concentration of 10wt.% PVA to water was used.

2.2.2. Manufacturing

Mixing Mixing of binder and iron (1.5vol.%) was carried out in a cylindrical glass bottle on a roller mixer (CAT, Germany) at 80 rpm for 30 minutes. Hereafter, urea was added to the glass bottle to create space holder volume fractions of 20%, 40% and 60 % and mixed for another 60 minutes. The volume fractions were calculated using Equation 2.1, where m_m, ρ_m and m_{sh}, ρ_{sh} are the masses and theoretical densities of iron powder and urea added to the matrix, respectively. The mixing resulted in six scaffold configurations; 20% volume porosity with coarse pores (2C), 20% volume porosity with fine pores (2F), 40% volume porosity with coarse pores (4C), 40% volume porosity with fine pores (4F), 60% volume porosity with coarse pores (6C) and 60% volume porosity with fine pores (6F). An schematic overview can be found in Figure 2.3.

$$x = \frac{m_{sh}/\rho_{sh}}{m_m/\rho_m + m_{sh}/\rho_{sh}} \tag{2.1}$$

Compaction Compaction of mixtures was conducted with a uniaxial powder press (Carver, USA). The mixture was cold-compacted (370 MPa) in a 13 mm diameter die (Carver, USA), filled with the same volume of mixture every time, creating green compacts of roughly 4 mm high. Compaction time was set at 5 minutes.

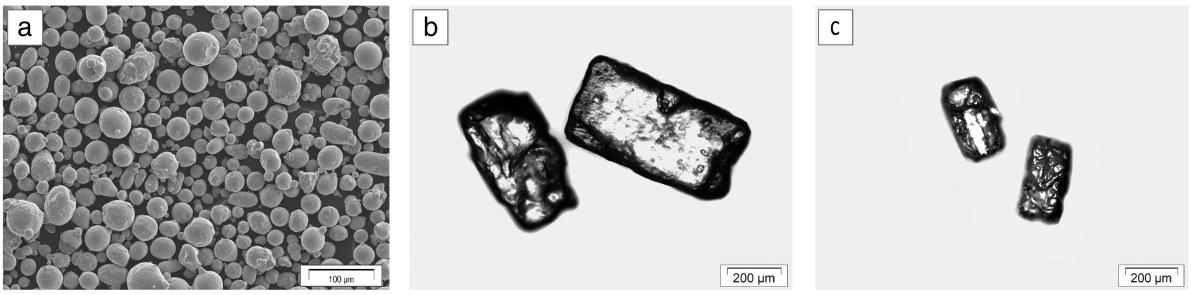

Figure 2.2: Sizes and shapes of powders: (a) iron powder, (b) large urea and (c) small urea

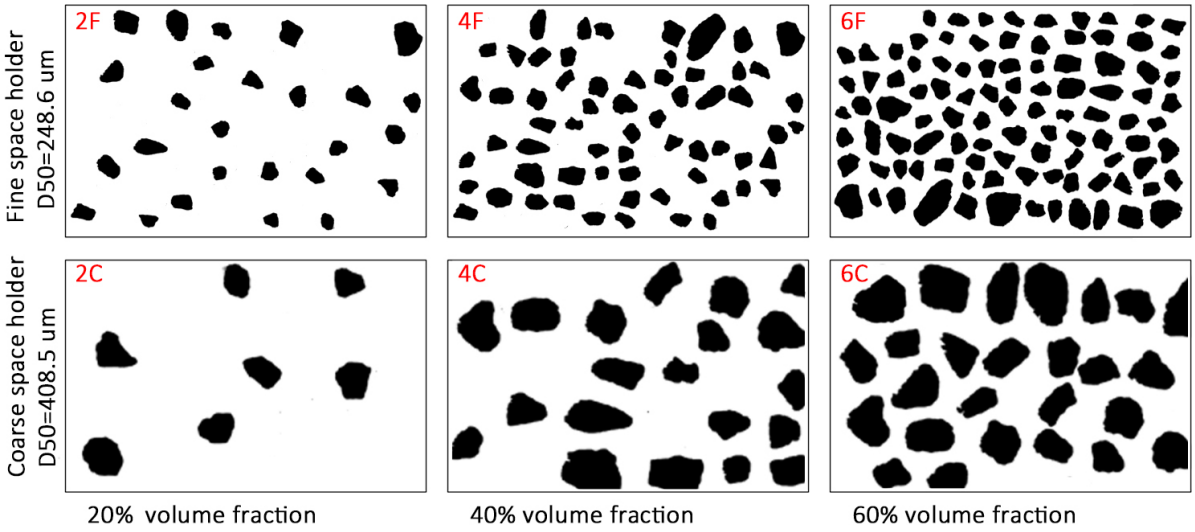

Figure 2.3: Fabricated scaffolds with their abbreviation

Leaching Leaching is the process of removing space holders to form a porous structure of metallic powder particles. Urea is easily dissolved in water, therefore the leaching process was performed in room temperature demineralized water for 20 minutes.

Sintering Sintering was performed in an STF 16/180 tube furnace (Carbolite, UK) with a low overpressure of 6.0 argon gas (purity $\geq$ 99.9999%). Prior to sintering the furnace was flushed with argon gas for 1 hour. A ramp rate of 2 °C/minute, sintering temperature of 1200 °C and sintering time of 4 hours were used. After sintering the furnace was turned off and natural cooling took place (average cooling rate of 2.5 °C/minute from 1200°C to room temperature).

All scaffolds were cleaned after sintering using sonication in 96% ethanol for 30 minutes, after which they were dried in open air.

2.3. Scaffold characterization

2.3.1. SEM and EDS

To examine morphologic characteristics of scaffolds, i.e. necking formation, pore sizes and pore quantity on scaffold surface, a scanning electron microscope (SEM) (JSM-IT100, JEOL, Japan) was used. SEM was equipped with energy-dispersive X-ray spectroscopy (EDS) which was used for chemical characterization of iron scaffold surface and corrosion products.

2.3.2. X-ray microtomography

Iron scaffolds were imaged using micro-computed tomography (μCT) (Phoenix Nanotom, GE Sensing Inspection Technologies GmbH, Germany) at a tube current of 220 μA, a tube voltage of 130 kV, 1440 projection with an exposure time of 500 ms resulting in a resolution of 10 μm. Images were reconstructed and converted into a series of 2D images (DICOM stack) using Phoenix Datos|x 2.0 (GE Sensing & Inspection Technologies GmbH, Germany). As can be seen in Figure 2.4a every scan contained three scaffolds. To get this image into quantifiable data several steps were taken:

1. An image series of one scaffold was copied and pasted out of the three scaffolds in a scan. Using open-source ImageJ 1.51h [38] (US National Institutes of Health, USA) software with plugin *Untilt Stack* the scaffold was tilted in an upright position. With plugin *Crop (3D)* this scaffold was cropped to a 5x5x2.5mm volume, as shown in Figure 2.4b with an xy (top), yz (side) and xz (front) view.

2. After using auto threshold, with pores being black, the binary images were improved by using plugin *MorphoLibJ*. Morphological 3D filters as opening and closing, with an octahedron as structural element, with a radius of 1 voxel, were applied, as shown in Figure 2.4c with a top and side view.

3. To assess interconnectivity between large pores, morphological segmentation of pores was performed using the watershed algorithm [27, 39, 40] of plugin *MorphoLibJ*. This procedure identified pores as individual items, which allowed additional information like pore volume, pore area, pore position and pore orientation to be calculated. Labels with a size $\leq$ 1000 voxels (0.001 mm^3) were removed to simplify subsequent calculations. Segmented volume shown in Figure 2.4d as a top and side view and in Figure 2.4e as 3D view.

4. Using plugin *MorphoLibJ*, the 3D regions were analyzed for volume (counting number of voxels that constituted a label weighted by the volume of an individual voxel), area (counting number of voxels that constituted a label weighted by the area of an individual voxel), inertia ellipsoid (filling a pore with an ellipsoid and returning i.a. its corresponding elevation angle) and size of the bounding box enclosing individual pores (of which the diagonal (L_{BB}) is used to describe the pore size).

Scans were made of cleaned scaffolds before and after immersion tests.

2.3.3. Archimedes test

To measure the interconnected porosity of samples, the ASTM standard B963-13, with Archimedes' principle, was used. For the purpose of this test a sample holder was designed and fabricated to measure the mass of scaffolds both in air and ethanol (purity of 96% and ρ_e=0.7895 g cm^{-3}) in an accurate manner, see Figure 2.5. The mass of sample holder was tared. Using an analytical balance (1801 MP, Sartorius GmbH, Germany) scaffolds were weighed in air (m_a). Thereafter scaffolds were impregnated with corn oil (ρ_o=0.9153 g cm^{-3} and viscosity of 64.68 cSt at room temperature [41]) in a vacuum (1.8 kPa) for 30 minutes and further immersed for another 30 minutes in corn oil at atmospheric pressure. Then, scaffolds with corn oil inside pores were weighed in air (m_{ao}) and in ethanol (m_{eo}).

Volume percentage of interconnected porosity (P) (as measured by oil impregnation) was then calculated with Equation 2.2.

$$P = \frac{\rho_e}{\rho_o} \frac{m_{ao} - m_a}{m_{ao} - m_{eo}} \tag{2.2}$$

2.3.4. Diametral compression test

Since height-to-diameter ratio of the scaffolds is 0.3 instead of the required ratio between 1 and 2 for a uniaxial compression test (ISO 13314:2011), diametral compression tests were used to determine the elastic moduli and yield strengths. To accommodate the diametral compression tests (ASTM D3967-08 standard), steel bearing blocks were fabricated by milling, see Figure 2.6.

Every scaffold was measured in threefold for both diameter and height using a caliper (Mitutoya, Japan). Bearing blocks were placed in a universal material testing machine (LR5K, Lloyd Instruments Ltd, UK) with a 5 kN load-cell. Measurements were performed after a pre-load of 0.5 N using a cross head displacement speed of 0.5 mm/min till a total deflection of 4 mm. The force-displacement plot was converted to a stress-strain diagram by Equation 2.3 and Equation 2.4 [42], with F being the compression force, H being the height of the scaffold, D_0 being the initial diameter of the scaffold, d_y being the cross head displacement and σ, ϵ being the stress and strain, respectively.

Based on the analysis of the linear slope in the elastic region (starting from 1 Pa to compensate for the setting of the scaffold in bearing blocks) of the stress-strain diagram, elastic modulus E and yield strength σ_y of the scaffold were determined.

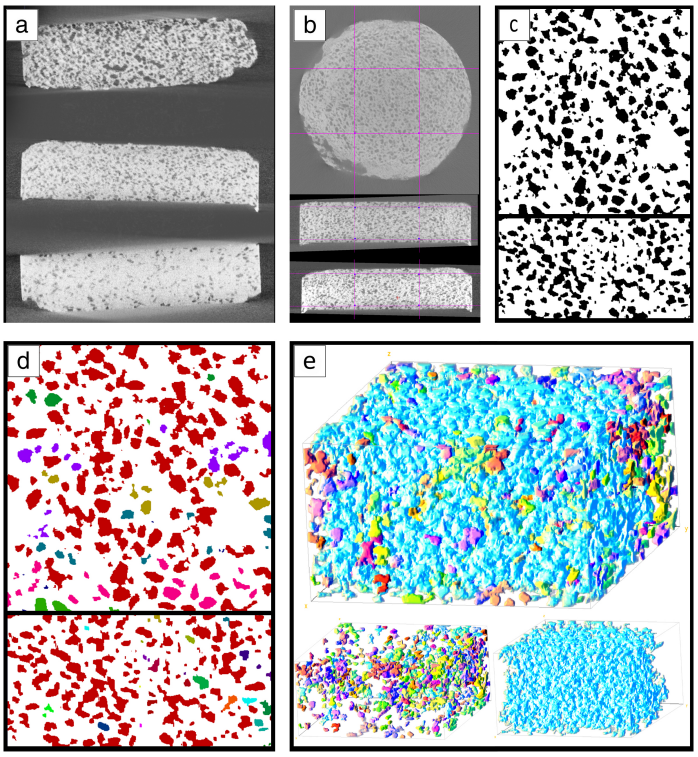

Figure 2.4: Processing steps of μCT data. a: original stack of three scaffolds, b: rotated and cropped to one scaffold xy, yz and xz view, c: cropped to ROI of 5x5x2.5mm and made binary xy and yz view, d: pores segmented xy and yz view, e: 3D volume rendering, bottom left without the largest pore, bottom right only showing the largest (interconnected) pore

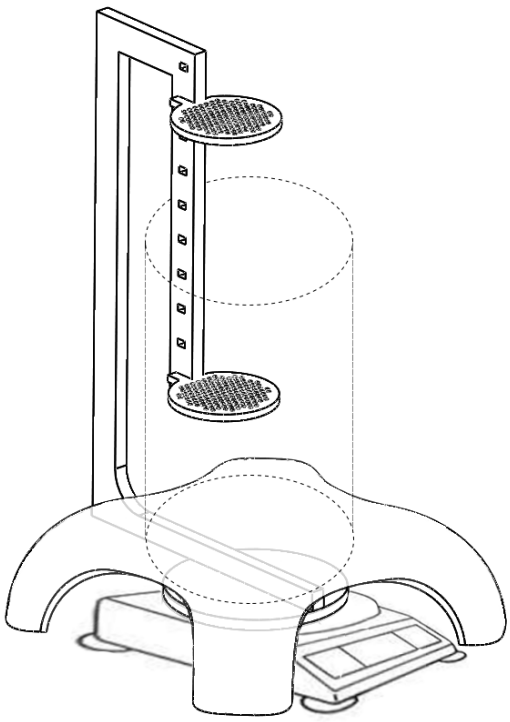

Figure 2.5: Sample holder for Archimedes' measurement

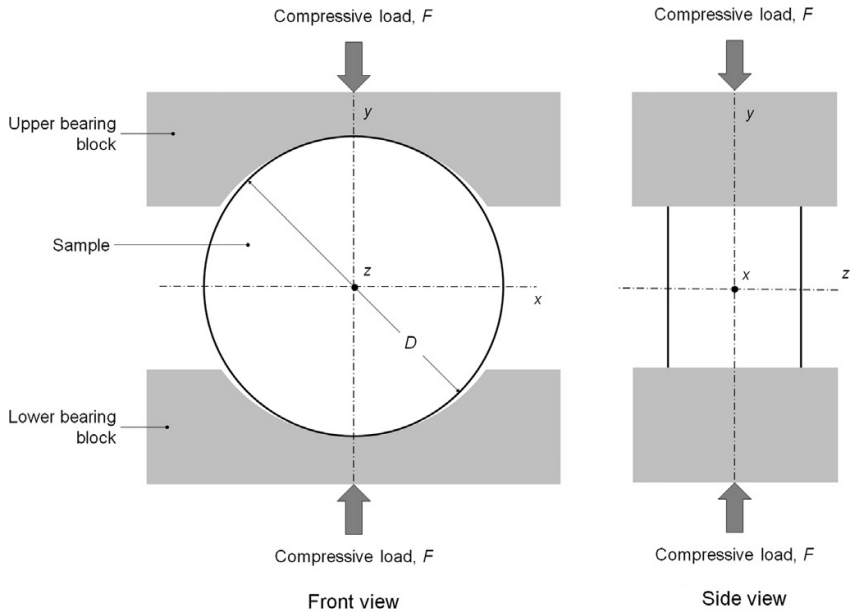

Figure 2.6: Diametral compression test [42]

2.4. Immersion tests

In vitro corrosion tests were conducted, roughly following the guidelines ASTM standard F3268-18a, in modified simulated body fluid (m-SBF) [43], see Table 2.1 listing ion concentrations. Upon creating, the pH of m-SBF was measured at 7.4 at 37 °C. All scaffolds were weighed using an analytical balance (1801 MP, Sartorius GmbH, Germany).

The setup shown in Figure 2.7 was designed and fabricated by laser cutting 4 mm poly methyl methacrylate (PMMA). Placed inside 2 L open beakers this created a ratio of 150 mL m-SBF per gram of iron scaffold. Three beakers, holding a total of 18 scaffolds, were placed inside a thermostatic bath (Corio, JULABO GmbH, Germany) at 37 °C. Each beaker was connected using tubes to a peristaltic pump (Gilson Minipuls 3, Meyvis, The Netherlands) keeping a flowrate of approximately 1.2 ml/min (within the range of fluid flow rate in bone marrow 0.012–1.67 mL/min [44]).

Immersion tests were conducted for durations of 3 and 11 days (3d and 11d). During the experiments temperature and pH of the m-SBF were measured using a pH bench meter (SevenExcellence, Mettler Toledo, USA). Simultaneously water levels of m-SBF and the thermostatic bath were checked and if needed demineralized water was added.

After immersion the scaffolds surface were inspected using SEM and EDS (JSM-IT100, JEOL, Japan). Thereafter all scaffolds were cleaned by lightly brushing, 1 minute sonication in 18.23% hydrochloric acid and 10 minutes sonication in 96% ethanol, after which the scaffolds were dried at room temperature. The scaffolds were weighed using an analytical balance (1801 MP, Sartorius GmbH, Germany) and reported in weight loss percentage. Furthermore, scaffolds were inspected using SEM, EDS (JSM-IT100, JEOL, Japan) and μCT (Phoenix Nanotom, GE Sensing & Inspection Technologies GmbH, Germany) and mechanical properties were measured using diametral compression tests.

$$\sigma = \frac{6F}{\pi H D_0} \tag{2.3}$$

$$\epsilon = \frac{\Delta d_y}{D_0} \tag{2.4}$$

Table 2.1: Nominal ion concentrations of m-SBF in comparison with human blood plasma [43]

Ion	Blood plasma (mM)	m-SBF (mM)
Na^+	142.0	142.0
K^+	5.0	5.0
Mg^{2+}	1.5	1.5
Ca^{2+}	2.5	2.5
Cl^-	103.0	103.0
HCO_3^-	27.0	10.0
HPO_4^{2-}	1.0	1.0
SO_4^{2-}	0.5	0.5

2.5. Electrochemical tests

For electrochemical testing, scaffolds were mounted in epoxy resin, sanded and polished up to 1 μm. Thereafter scaffolds were cleaned using 96% ethanol and dried in open air. Copper screws were drilled into the resin to make the samples conductive, see Figure 2.8. For this test the same m-SBF as mentioned in Section 2.4 was used.

Electrochemical tests were performed using a three-electrode cell with graphite as counter electrode, Ag/AgCl as reference electrode and the iron scaffold as working electrode. As can be seen in Figure 2.8, the working electrode was immersed 1 mm in m-SBF to prevent it from penetrating the porous scaffold all the way to the copper screw. The three electrodes were placed inside a glass beaker containing 200 mL m-SBF at room temperature, creating a solution to sample surface area of approximately 180 mL per cm^2. The complete setup was placed inside a Faraday cage.

Before starting potentiodynamic polarization the setup was first stabilized for 2.5 hours to reach open circuit potential (OCP). Then polarization started at an initial potential of 0.35 V below OCP and was increased to 0.5 V above OCP at a scan rate of 0.5 mV/s.

The exposed area was determined after measurements and was calculated by importing an image of the scaffolds embedded in resin, shot by a stereo microscope (SZX9, Olympus, Japan), into ImageJ [38]. After normalizing for surface area the polarization curves were plotted and the corrosion current density was calculated by the Tafel extrapolation method [45].

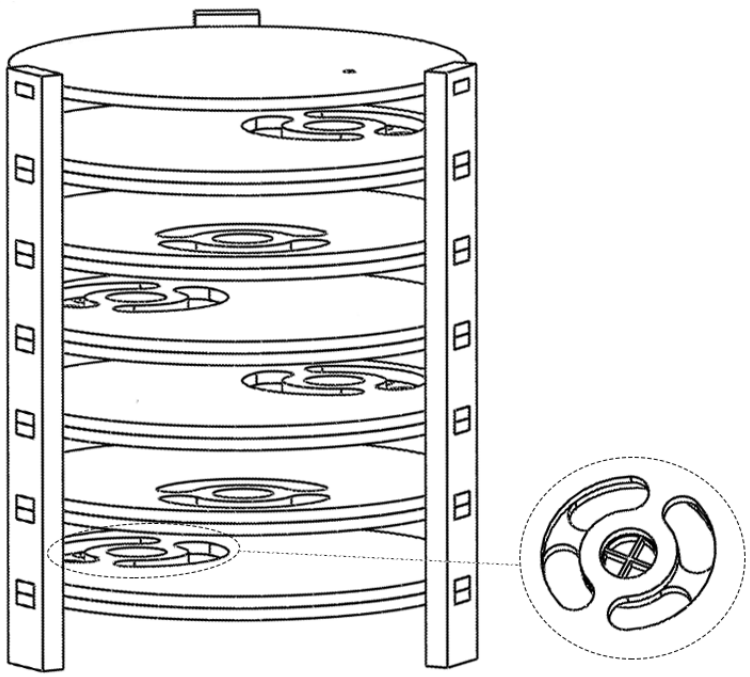

Figure 2.7: Sample holder for immersion in m-SBF

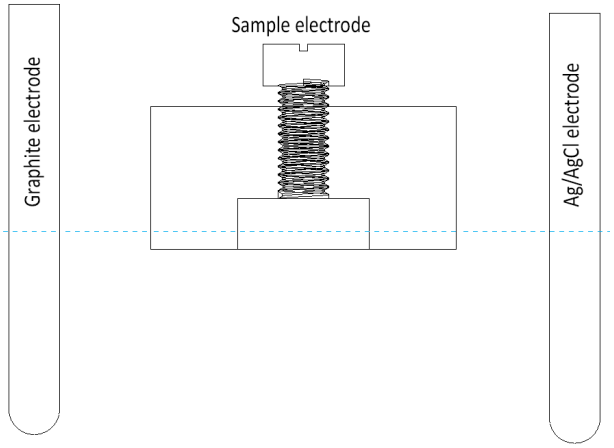

Figure 2.8: Setup for electrochemical test in m-SBF

2.6. Statistical analysis

Graphical results were presented in mean ± standard deviation. Statistical analysis was determined with GraphPad Prism (GraphPad Software, La Jolla, California, United States) using one-way ANOVA tests. Statistic significant between groups were considered at $p \leq 0.05$.

3

Results

3.1. Anterior scaffold characterization

3.1.1. Surface characterization

The surface of the created scaffolds is porous, see Figure 3.1. Outer pores show the same shape characteristics as urea in Figure 2.2b-c. An increase in space holder volume fraction clearly shows an increase in porosity, Figure 3.1a-c-e and Figure 3.1b-d-f. First signs of interconnected pores can be spotted at 4C and 4F, but fully interconnected pores are mainly spotted at 6C and 6F. At 6C and 6F, agglomeration of space holder particles can be spotted by the different shape of the created pores, see Figure 3.1e-f, where mainly fine space holders have a tendency of agglomerating and creating new pore shapes.

There is minimal necking between iron particles at the sample surface and both pore size and pore quantity do not seem to affect it, see Figure 3.2. Addition of space holders does not seem to influence necking, meaning that there is no difference in micro porosity between the different configurations at sample surface, see Figure 3.2.

3.1.2. Porosity

Archimedes' test and μCT were used to determine the porosity of samples, however, Archimedes' test only shows the interconnected porosity and is performed using oil immersion which can cause measurement error. Furthermore, μCT calculation is done using only an inner ROI, whereas Archimedes' test uses the complete sample, including outer pores and imperfections near the surface. That being said both Archimedes' test and μCT measured a lower porosity than expected, see Figure 3.3. At an expected porosity (volume fraction) of 20%, the largest deviation came from the coarse scaffold at a porosity of 13.4% measured by μCT, see Figure 3.3 and Table 3.1. This maximum deviation from the expected porosity increased a bit at 40% where fine scaffold is at 28.7% porosity measured by μCT. At an expected porosity of 60% the deviation becomes the largest at 36.6% porosity again measured by μCT, see Figure 3.3 and Table 3.1. All Archimedes' measurements stay within 10% of the expected values. There is no significant difference between measured coarse and fine values and the correlation between space holder volume fraction and measured porosity is nearly linear.

More specific information about how the porosity is built up can be found in Table 3.1. The number of individual pores found is the highest for 2F, meaning that this sample shows a lot of small isolated pores. The lowest number of individual pores was found in configuration 6C, caused by interconnection of pores. The interconnection is shown as pore connectivity in Table 3.1 and was calculated by dividing the largest pore volume by the total pore volume. At configurations 6C and 6F, almost 95% of porous volume consist of one large interconnected pore. Samples of lower porosity show that pore connectivity is higher when using fine space holders. The total area of porous network follows the same trend, where 2F and 4F have larger areas compared to 2C and 4C. At 6F agglomerations of these fine space holders are causing a drop in surface area compared to 6C.

Every individual pore was also measured by the diagonal of its bounding box, however, one should be careful comparing these values. Interconnected pores are counted as one, so when looking at the mean value of all those diagonals, a smaller value does not necessarily imply smaller pores. It rather implies

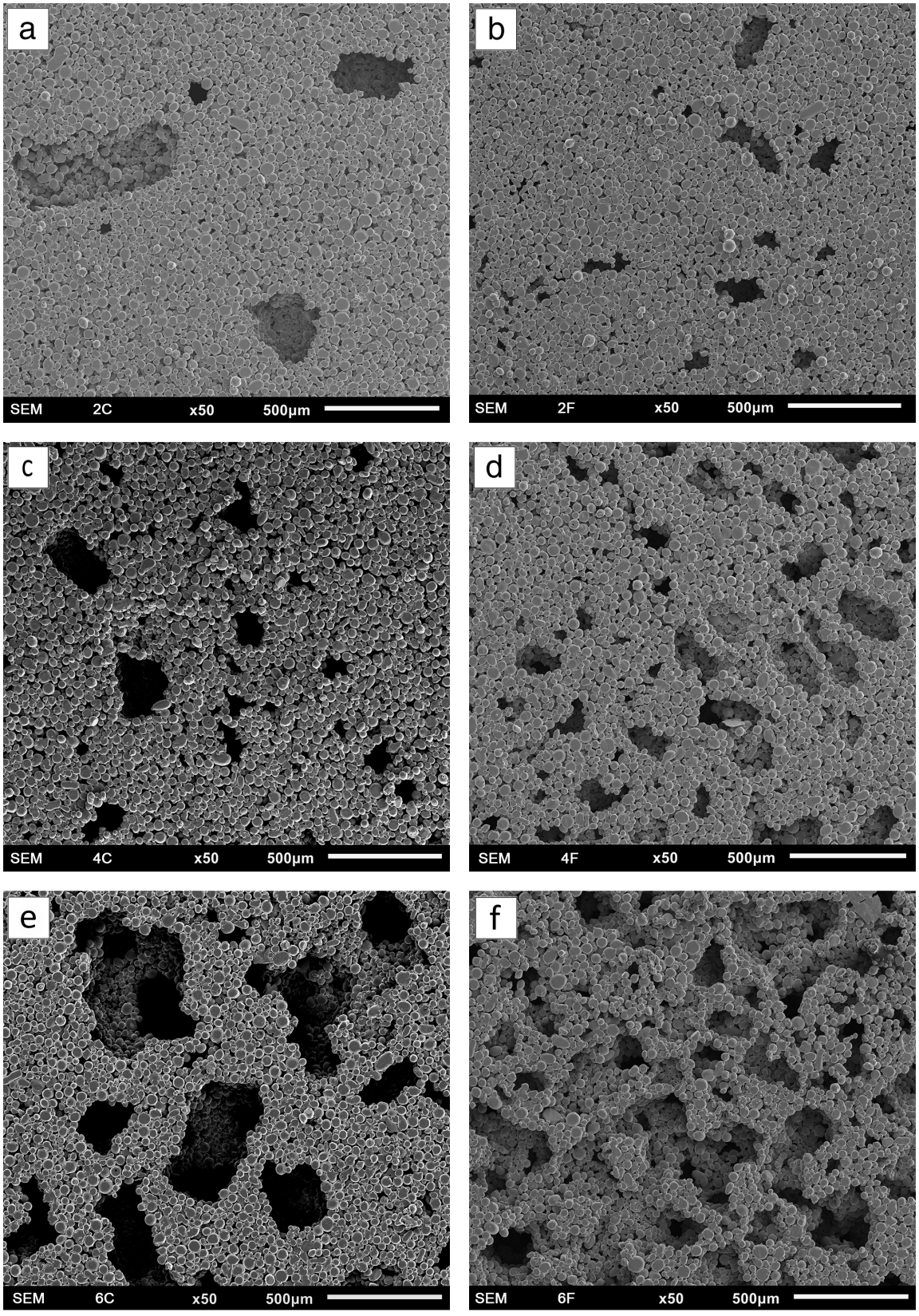

Figure 3.1: SEM images at 10 kV with 50 times magnification. a: 2C, b: 2F, c: 4C, d: 4F, e: 6C, f: 6F

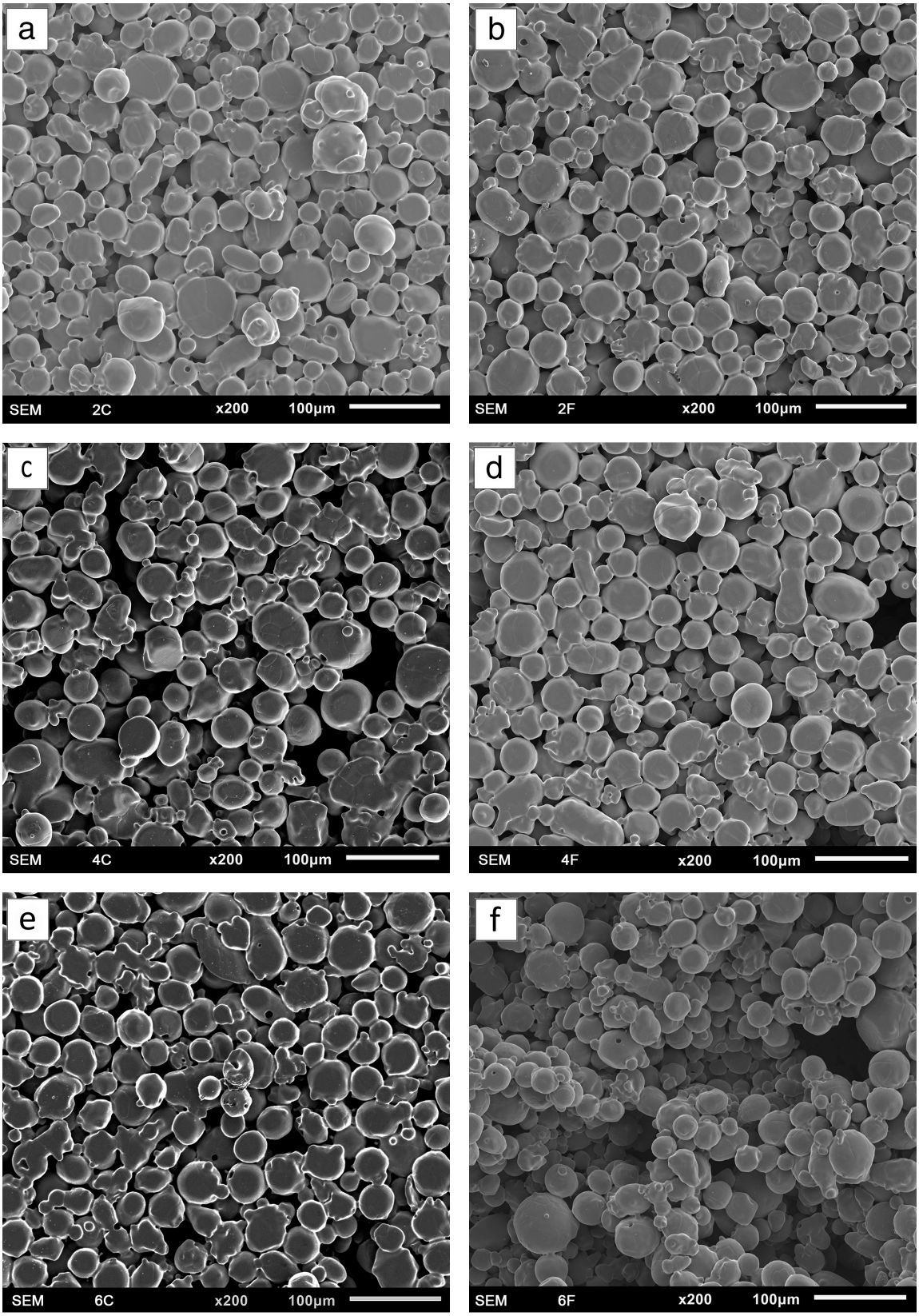

Figure 3.2: SEM images at 10 kV with 200 times magnification. a: 2C, b: 2F, c: 4C, d: 4F, e: 6C, f: 6F

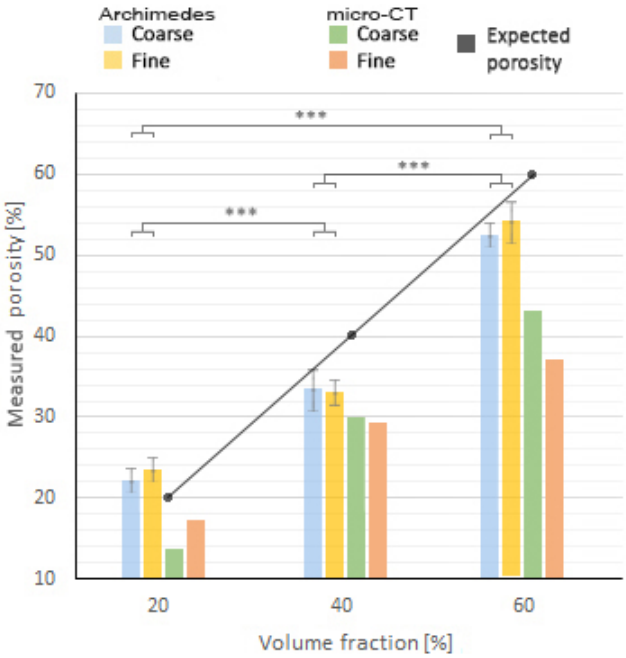

Figure 3.3: Measured porosity versus volume fraction. Black line shows the ideal line, Archimedes' shows mean (n=3) and SD, μCT shows mean (n=1). *** p≤0.001

that there is a large number of isolated small pores, specifically if pore connectivity is high. However, for samples 2C and 2F, pore interconnectivity is not at a high level. With Table 3.1 and Figure 3.4, the mean size and size distribution of isolated coarse and fine pores can clearly be distinguished.

Similar to the bounding box, ellipsoid measurement only uses individual pores, meaning that the altitude angle is dominated by smaller isolated pores and does not represent large interconnected pores. Nonetheless, all smaller isolated pores show a large preference to move in a plane perpendicular to the applied compaction pressure, see Table 3.1. This preference is so large that it can also be observed at the cross section of xz and zy plane in Figure 3.5. This also shows that even large interconnected pores display preference of space holders to move in this plane.

The higher pore connectivity of 2F and 4F compared to 2C and 4C can also be observed in Figure 3.5. Sample 6F, however, shows a turning point, due to agglomeration of fine space holder particles larger pores are more, making 6F more similar to 6C. This causes 6F to have a lower surface area than 4F, see Table 3.1. Figure 3.5 also shows small pore throats (interconnection channel between pores), although pore connectivity is high, permeability might be low due to these small pore throats. The earlier mentioned correlation between volume fraction and porosity is also observed in strut thickness. A reduction of strut thickness, with increasing volume fraction of space holders, is shown in Figure 3.5.

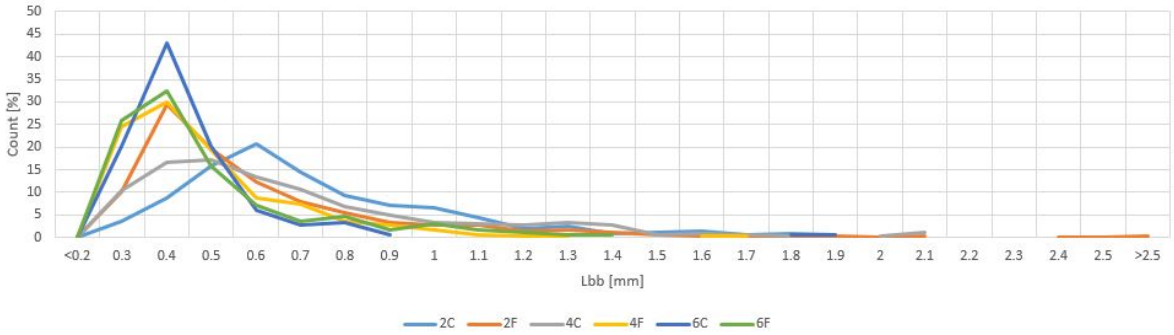

Figure 3.4: Pore size distribution by count percentage on bounding box diagonal of individual pores

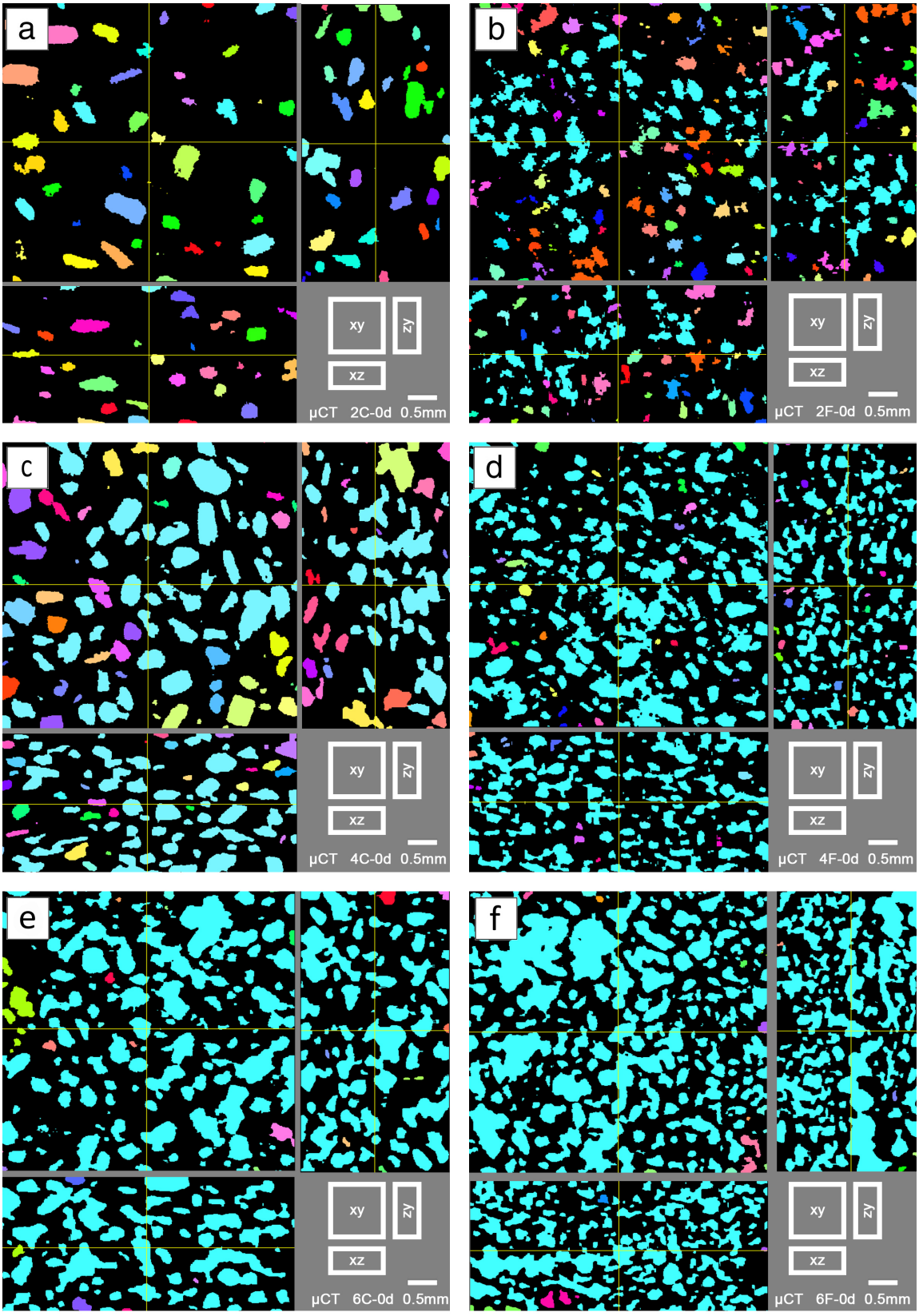

Figure 3.5: Cross sectional μCT view in the xy, zy and xy directions (planes are on yellow lines), each individual (segmented) pore is color coded. a: 2C, b: 2F, c: 4C, d: 4F, e: 6C, f: 6F

Table 3.1: General porosity information by μCT

Sample	# Pores	Porosity (%)	Pore connectivity (%)	V_{tp} (mm^3)	A_{tp} (mm^2)	L_{BB} (mm)	Pore fraction ϕ^a <30° (%)
2C	375	13.4	3.5	8.37	193.57	0.70	70.9
2F	795	17.1	32.4	10.71	390.00	0.56	56.1
4C	337	29.4	56.1	18.40	403.33	0.68	71.5
4F	447	28.7	88.3	17.94	590.02	0.46	63.3
6C	149	42.4	97.1	26.51	651.16	0.47	55.7
6F	170	36.6	94.9	22.85	494.83	0.51	65.9

V_{tp} = total volume of porous network / A_{tp} = total area of porous network / L_{BB} = diagonal of bounding box
^{a} Elevation angle of ellipsoid

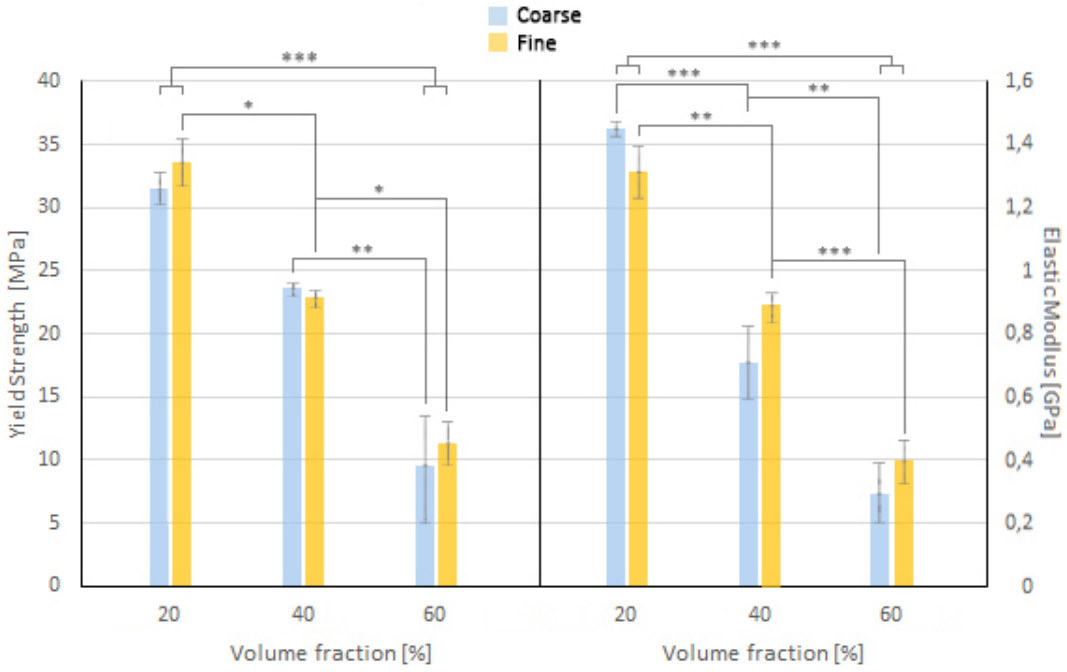

Figure 3.6: Strength and stiffness, shown by mean (n=3) and SD, of scaffolds measured by diametral compression. * p≤0.05, ** p≤0.01, *** p≤0.001

3.1.3. Mechanical behaviour

After the diametral compression tests both strength and stiffness values of all samples were calculated, as shown in Figure 3.6. Differences between coarse and fine porous structure are minimal and not significant, both for strength as for stiffness. However, the decrease in strength and stiffness for increasing porosity is significant. Stress-strain curves of all scaffolds can be found in Appendix B.

3.2. Corrosion of scaffolds

3.2.1. *In vitro* corrosion behavior

In vitro corrosion behavior was determined by immersing scaffolds in m-SBF and experiment durations were for 3 and 11 days (3d and 11d). During immersion temperature and pH were measured. Since m-SBF was heated indirect, by water flowing around the beakers, it took a while before m-SBF reached the desired temperature of 37 °C. During the increase in temperature, pH also increased, as shown in Figure 3.7. After the first day, temperature was constant but pH kept increasing at a slow rate till 7.53, resulting in a pH increase of 0.08 in 10 days.

After an immersion time of 3 and 11 days the scaffolds were taken out of m-SBF and inspected, see Figure 3.8. Brownish corrosion products appeared on scaffold surface after 3 days. The layer of

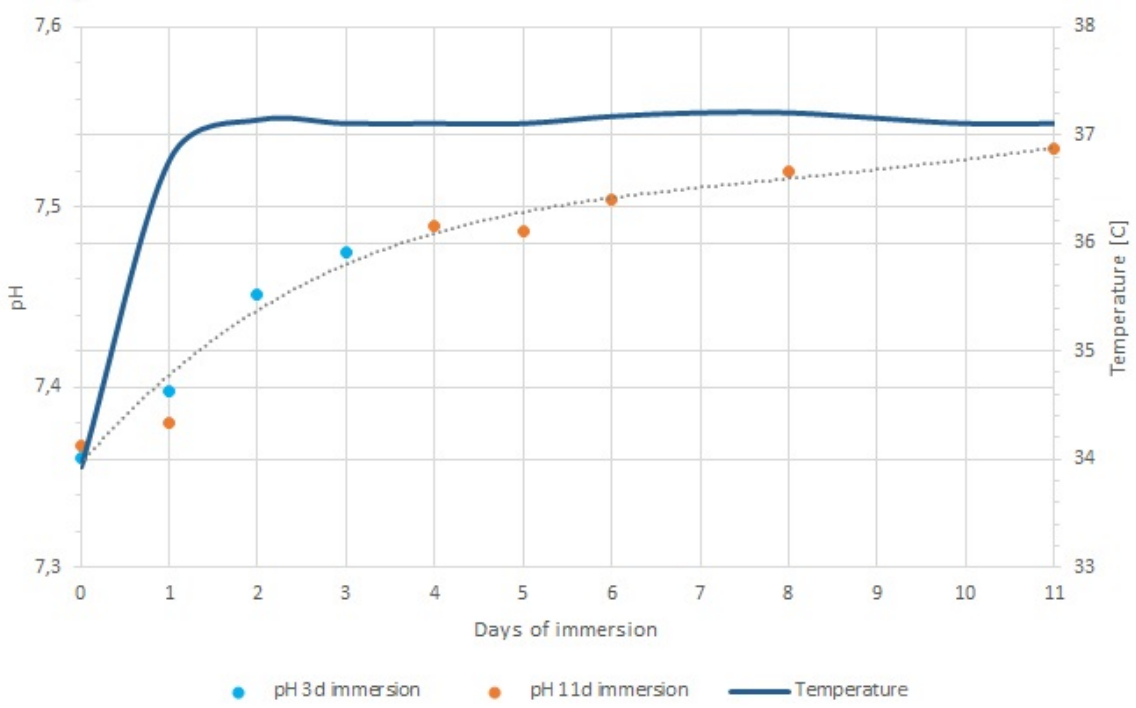

Figure 3.7: Temperature and pH variations of m-SBF during immersion of scaffolds

corrosion products increased to a thicker and more covering layer after 11 days of immersion. A more in depth inspection of corrosion products was performed using SEM and EDS, see Figure 3.9. This shows that corrosion products mainly consist of iron, although when compared to non-corroded parts, see Figure 3.9c-d, iron was 50% lower in mass percent due to an increase in mainly oxygen. Traces of carbon, nitrogen, phosphorus and calcium were also found in corrosion products. There is no clear difference between corrosion products of fine or coarse scaffolds, neither does the porosity change the elements of corrosion products, see Figure 3.9.

After cleaning, mass loss of every scaffold was measured, see Figure 3.10. After 3 days of immersion samples 2F, 2C, 4F and 4C show a weight increase. Samples 6C and 6F do show weight loss of 0.8% and 0.6% after 3 days of immersion. Weight loss becomes more significant at 11 days of immersion, especially for samples 6F and 6C who have a small significant difference with weight losses of 1.8% and 1.3%, respectivly.

Weight losses of coarse and fine samples are approximately the same, making space holder volume fraction of higher significance than space holder particle size for mass loss of iron scaffolds.

3.2.2. Electrochemical behavior

Corrosion current density values were calculated by using cathodic Tafel extrapolation, considering the non-symmetrical polarization curves between anodic and cathodic branches. The current density of all samples was between $2.75.10^{-6}$ $5.90.10^{-6}$ $A.cm^{-2}$, see Figure 3.11. No significant difference could be found for porosity or pore size. It is important to note that, since corrosion current density is normalized for contact area, this only indicates that for the different pore structures the corrosion rate per surface area does not change significant. The polarization curves can be found in Appendix B.

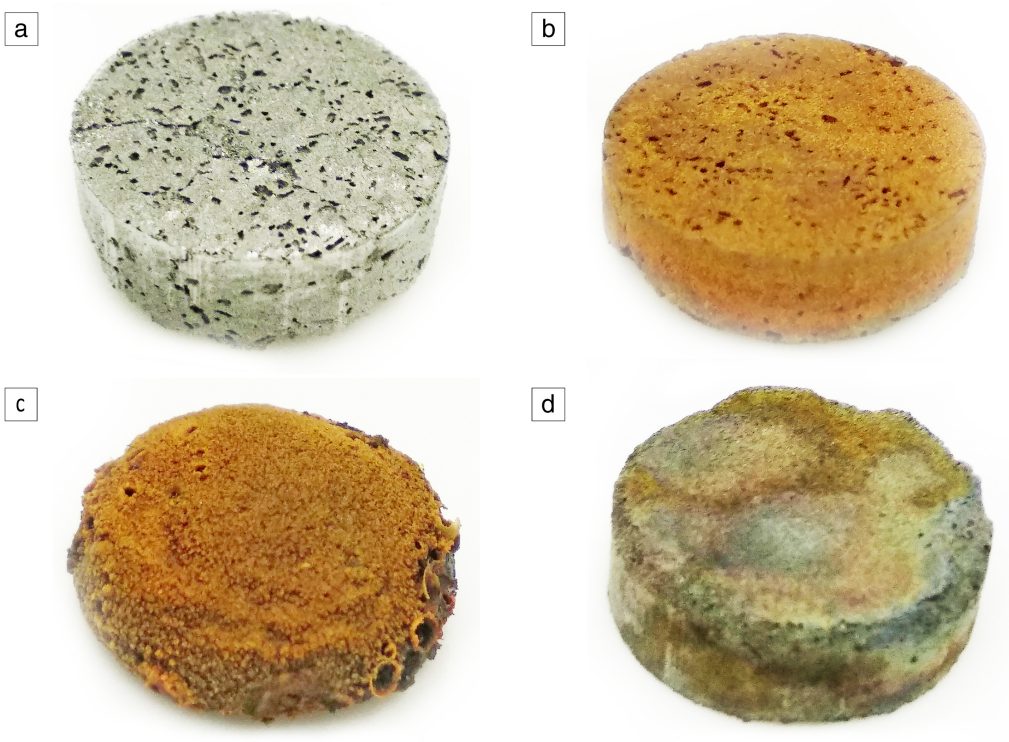

Figure 3.8: Porous iron scaffolds at different stages. a: initial scaffold before immersion (4C), b: scaffold after 3 days immersion (4C-3d), c: scaffold after 11 days of immersion (6C-11d), scaffold after immersion and cleaning (2F-11d)

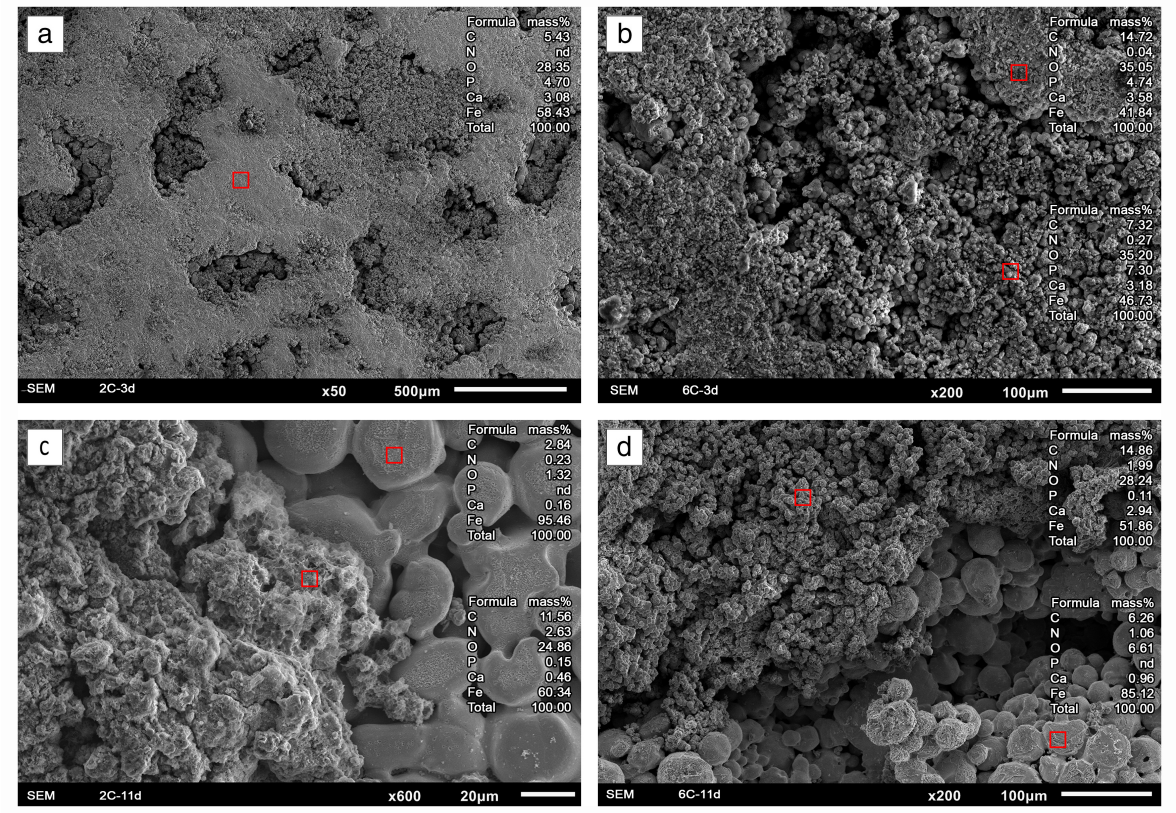

Figure 3.9: Elements present in corrosion products after scaffold immersion in m-SBF, presented by mass percentages and found by EDS in red square. a: 2C-3d, b: 6C-3d, c: 2C-11d, d: 6C-11d

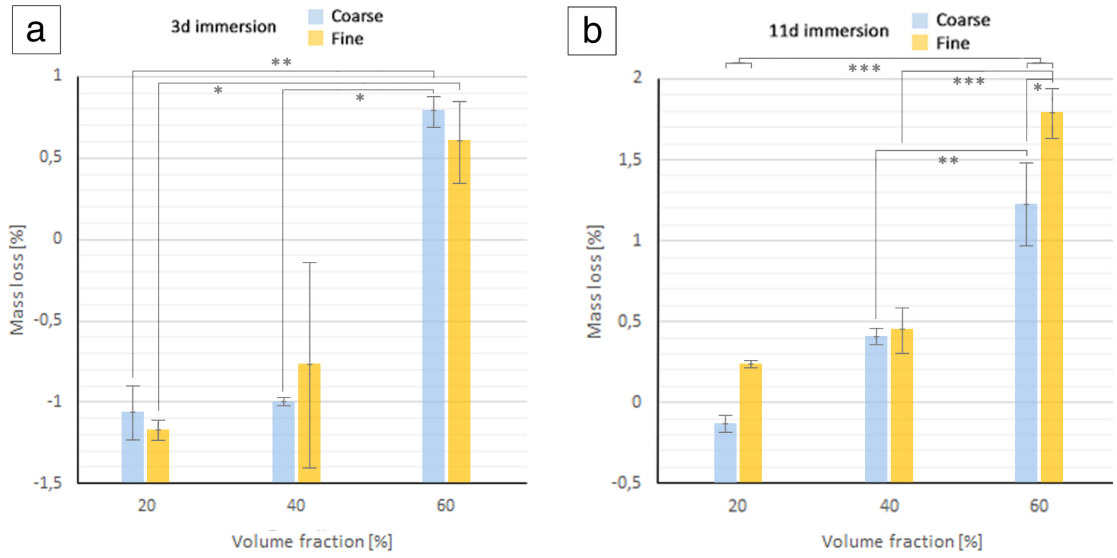

Figure 3.10: Mass loss, shown by mean (n=3) and SD, of scaffolds after immersion in m-SBF. a: 3 days immersion, b: 11 days immersion. * p≤0.05, ** p≤0.01, *** p≤0.001

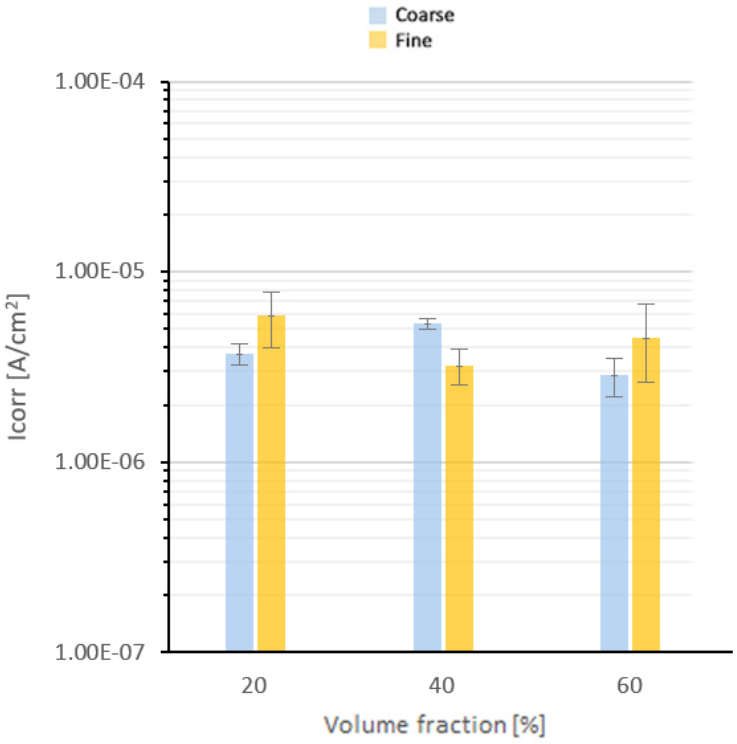

Figure 3.11: Corrosion current density, shown by mean (n=2) and SD

3.3. Posterior scaffold characterization

3.3.1. Surface characterization

After immersion and cleaning, samples surfaces were compared by SEM and EDS, see Figure 3.12 and Figure 3.13. Mass percentages of oxygen show that removing oxide is, mainly when porosity percentages get higher, quite difficult. All specimen show in some form retained corrosion products. This means that cleaning could have been more thorough. However, all specimen also show roughening of the surface. This is partly due to corrosion, but chemical cleaning also removes iron. Therefore, no further cleaning was performed. Addition of new elements to the corroded surfaces due to cleaning is negligible. No corrosion differences between coarse and fine pores were observed. However, differences between lower and higher porosities seem to influence corrosion. Higher porosities show a rougher surface and more remaining corrosion products between micro pores. The same increases in surface roughness and remaining corrosion products are observed when comparing samples after 3 days immersion and those after 11 days immersion test, see Figure 3.12 and Figure 3.13.

After surface characterization porosity measurements were performed by means of μCT, similar to Section 3.1. However, as can been seen in Figure 3.14, the influence of corrosion on pore area and pore volume of scaffolds is minimal. More extensive μCT data of samples after immersion created a data repetition of Table 3.1 and is therefore not presented.

3.3.2. Mechanical behaviour

After diametral compression tests both strength and stiffness of every sample were calculated, presented in Figure 3.15. Samples do not show significant differences, between strength and stiffness, of coarse and fine porous structures. However, the decrease in strength and stiffness due to an increased porosity is significant, see Figure 3.15. When starting with immersion, scaffold strength decreases which decreases further for a longer immersion time. During immersion the stiffness of the scaffolds changes minimally. Stress-strain curves of all scaffolds can be found in Appendix B.

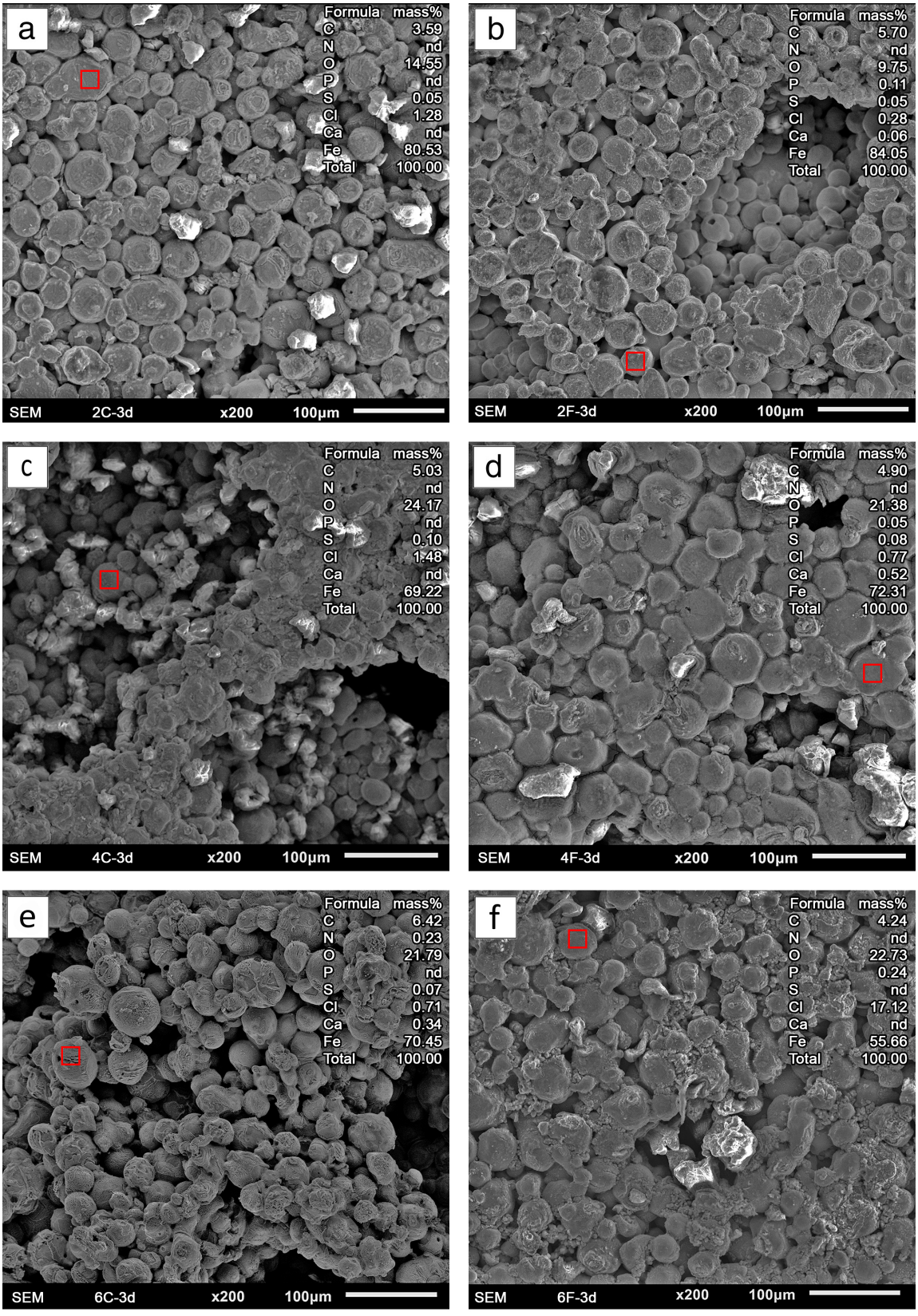

Figure 3.12: SEM images and EDS at 15 kV with 200 times magnification of cleaned scaffolds after 3 days immersion in m-SBF. a: 2C-3d, b: 2F-3d, c: 4C-3d, d: 4F-3d, e: 6C-3d, f: 6F-3d

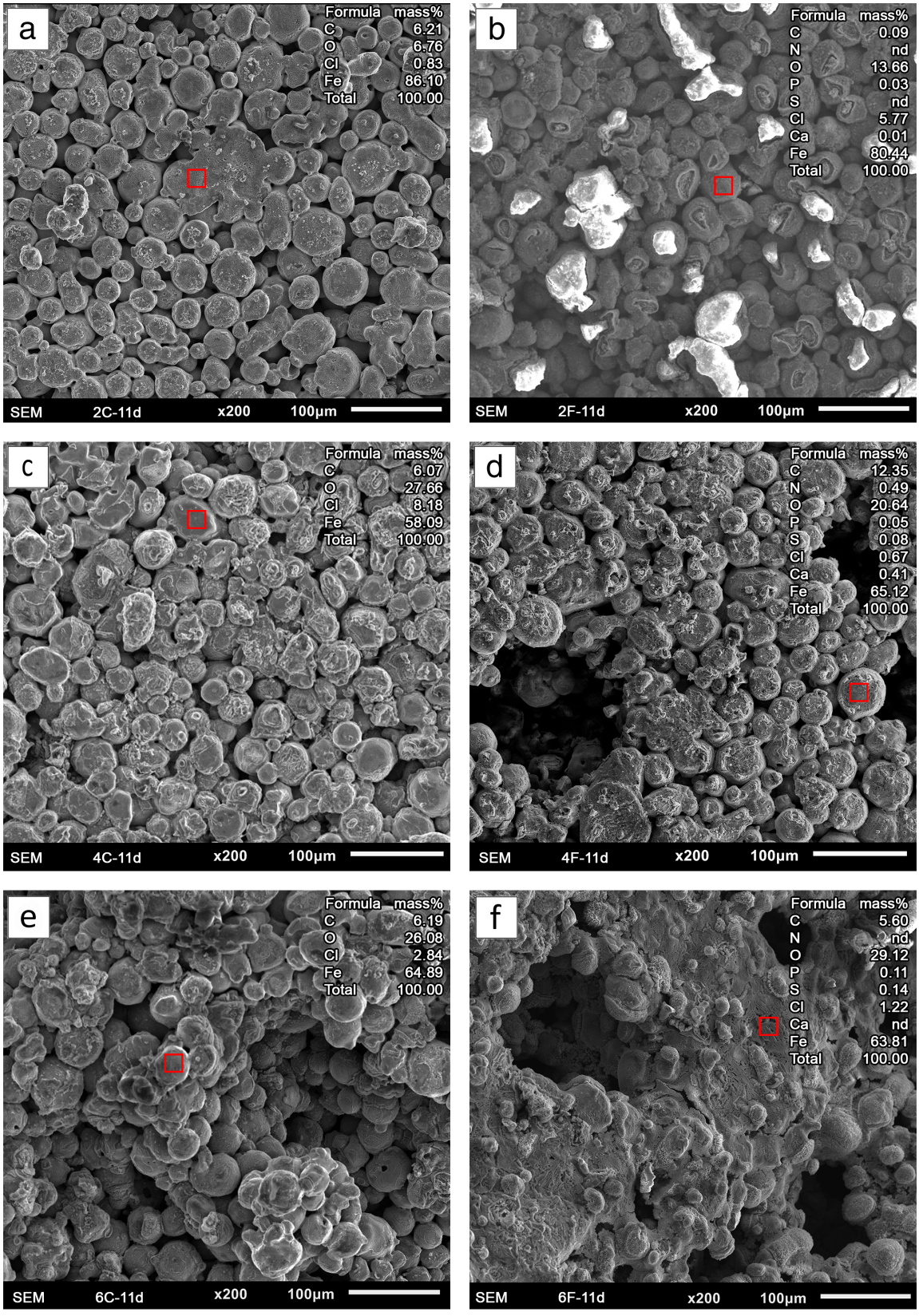

Figure 3.13: SEM images and EDS at 15 kV with 200 times magnification of cleaned scaffolds after 11 days immersion in m-SBF. a: 2C-11d, b: 2F-11d, c: 4C-11d, d: 4F-11d, e: 6C-11d, f: 6F-11d

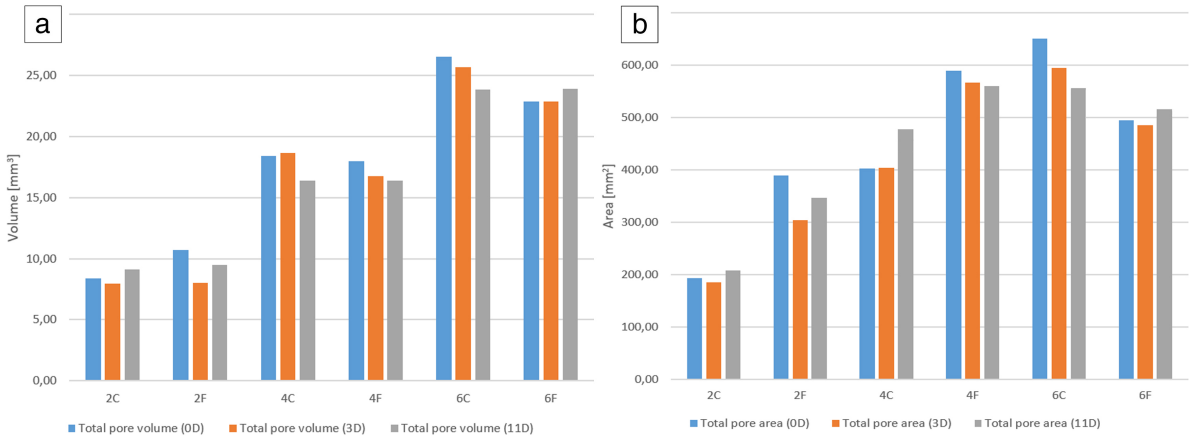

Figure 3.14: μCT data (n=1). a: total pore volume before immersion, after 3 days of immersion and after 11 days of immersion, b: total pore area before immersion, after 3 days of immersion and after 11 days of immersion

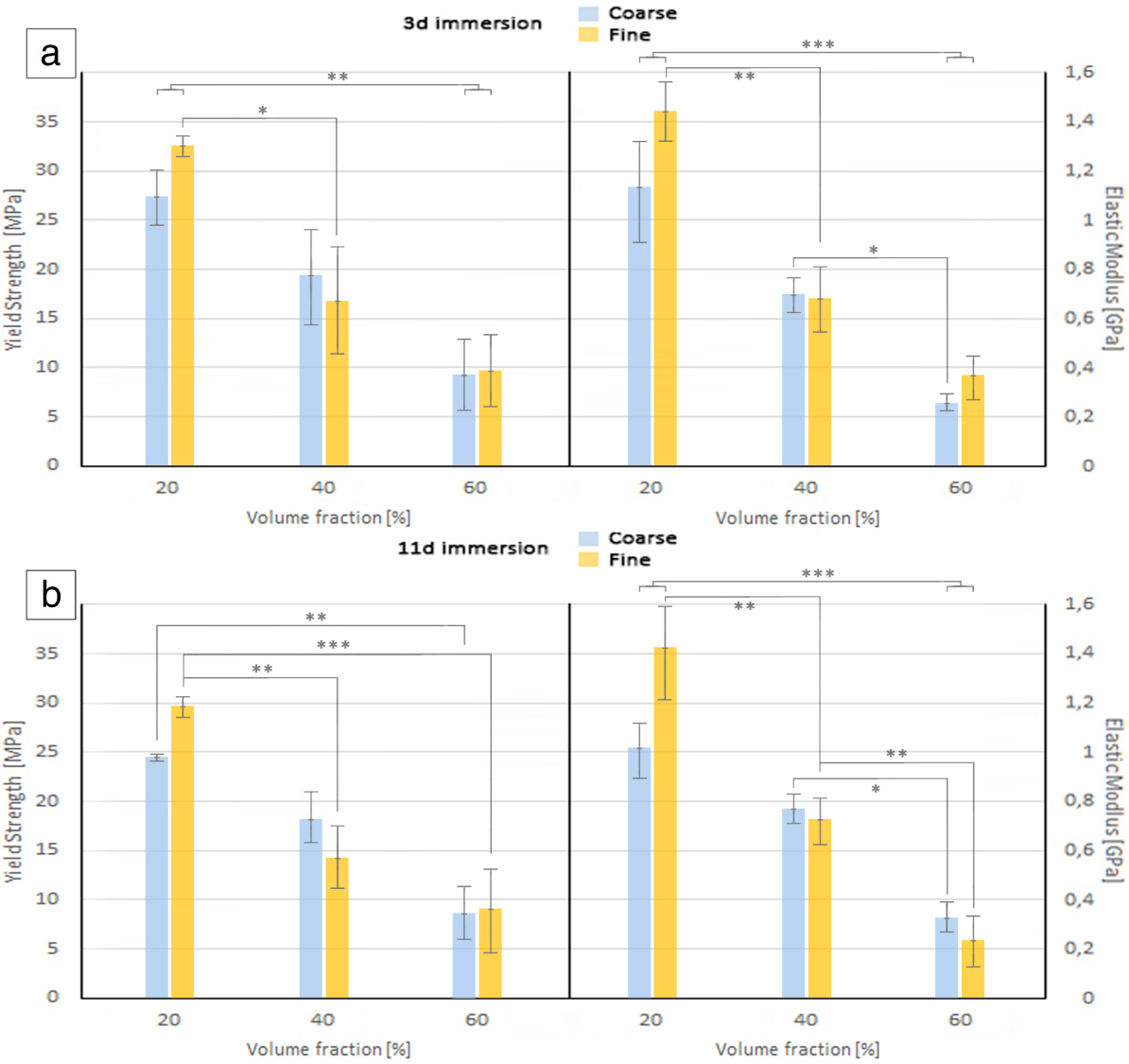

Figure 3.15: Strength and stiffness of scaffolds, shown by mean (n=3) and SD measured by diametral compression. a: after 3 days immersion, b: after 11 days immersion. * p≤0.05, ** p≤0.01, *** p≤0.001

4

Discussion

This study aims to define the effects of space holder particle size and volume fraction on the geometric characteristics and performance of absorbable iron scaffolds[1]. Using SHM six samples were fabricated; 2C, 4C and 6C, with coarse rectangular space holders (D_{50}=408.5 μm), and 2F, 4F and 6F, with fine rectangular space holders (D_{50}=248.6 μm), see Figure 2.3. After fabrication, SEM was performed to observe surface characteristics, μCT and Archimedes' tests were performed to quantify pore characteristics and diametral compression tests were performed to measure mechanical properties. Thereafter, immersion tests (3 and 11 days) and dynamic polarization tests were performed to observe corrosion and electrochemical behaviour. The effect of corrosion on the samples was characterized by performing SEM, EDS, μCT and diametral compression on the immersed samples.

4.1. Surface characteristics

Based on the SEM images, it is observed that the morphology of the final pores was similar to that of space holder particles. Pores can be designed, using SHM, by ensuring proper sizes and volume fractions of space holder particles. It can be stated that space holders played a key role in defining the pore structure of the fabricated scaffold. It is however important to note that, at higher porosities, the chance of agglomerating space holder particles becomes larger, creating differently shaped pores. At lower porosities (2C and 2F) pores represent the shape and morphology of the space holder particles. At higher porosities those pores become more connective (4C and 4F), or fully connected (6C and 6F). SEM images also showed micro porosity for all the samples, meaning that, although space holder particles were isolated, the pore network might in fact be connected through micro pores in the walls [46]. Micro porosity in orthopedic scaffolds is believed to help with proliferation and attachment of osteoblasts [4, 30] and is therefore desirable. Micro porosity on the other hand could act as initial crack in the matrix and highly influence the strength of a scaffold [21, 47]. In this study only external micro pores were examined, with no significant difference between samples. This is in contrast to Čapek et al. [34], who found that increasing the amount of space holder, leading to a relative increasing compaction of metal matrix powder, led to a decreasing amount of micro pores.

4.2. Topology characteristics

μCT images were used to observe the internal pore structure. Since urea is rectangular, the scaffolds did not have a well-defined pore structure and internal pores appear to randomly feed into each other, see Figure 4.1. According to the observations of Zhang et al. [48] spherical space holders create an ordered pore structure with well-defined interconnectivity. Furthermore, throat size (important for cell seeding and migration in scaffolds) seemed larger for spherical space holders [48]. Easier quantifiable μCT data were the number of individual, isolated pores in each sample. Sample 2F had almost five times more isolated pores than sample 6F, even though much more space holder particles are added to the latter. This suggests that pores become interconnected at higher space holder volume fractions. Bekoz and Oktay [46] suggest that, due to angularity of space holder particles, small interconnecting throats are

[1] The discussion of the effects SHM fabrication steps have on iron scaffolds can be found in Appendix A

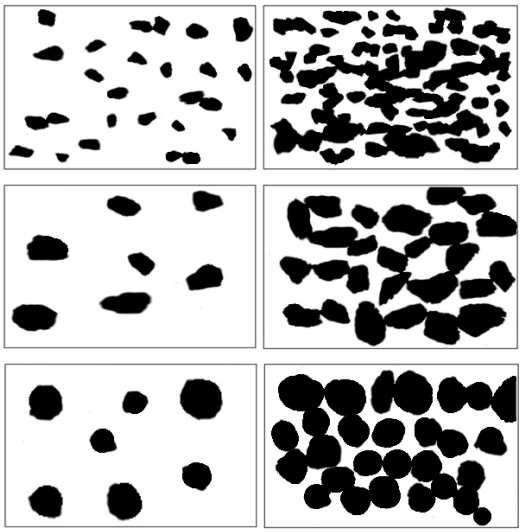

Figure 4.1: Schematic representation of how space holder size, volume fraction and shape form a pore structure.
Showing that smaller space holders have a higher tendency of agglomerating and thus creating a higher pore connectivity at low volume fractions yet also drop their higher area to volume ratio, compared to larger space holders, at higher volume fractions due to agglomeration. Showing that angular space holders have a tendency to move towards the plane perpendicular to the applied compaction pressure along with creating small interconnecting throats who randomly feed into each other, different from spherical space holders, who create an ordered pore structure with well defined pore throats.

created, which causes the number of isolated pores to decrease. Pore connectivity calculations confirmed this and showed how different sizes and volume fractions of space holder particles are affecting pore connectivity. Sample 2C had the lowest pore connectivity, efficient mixing caused uniform distribution of large isolated space holder particles. This changed for sample 2F, where, although with the same volume of space holder particles, the larger number of space holder particles caused a higher interconnection, this is schematically represented in Figure 4.1. Logically pore connectivity increases more for samples 4C and 4F because more space holders means a higher interconnection [46, 47]. The benefit of having smaller space holders (4F) compared to larger space holders (4C), in order to increase pore connectivity, is still valid at this fraction level. However, sample 6C and 6F have approximately the same pore connectivity. Although the general porosity still increased, higher interconnectivity for finer space holders is no longer observed. This finding can be explained by pore connectivity reaching its maximum value, similar to the findings of Cabezas-Villa et al. [39] where a pore connectivity of 99% is reached at 50% porosity. However, when comparing pore areas normalized by pore volumes of 6F and 6C, 6F turns out to give a lower area to volume ratio. This means that agglomeration causes fine space holder particles to form larger pores than coarse space holder particles do, meaning that space holder volume fraction do not only change porosity, but might also change pore size and shape, as schematically shown in Figure 4.1. This is in line with the observation in SEM images. It is important to note that this effect is more pronounced when using rectangular space holder, as a combination of large spherical space holders with smaller matrix particles leads more likely to separated macro pores [48]. Arifvianto et al. [49] observed a maximum surface area at 60% space holder fraction, when they compared coarse space holder fractions between 40% and 80%. Although not specifically mentioned, this probably is the same effect as the agglomeration phenomena in this study. This also explains why the trend of smaller space holders creating a larger surface area [50] ends at samples 6C and 6F. Since only three porosity values are checked, the ”turning point” at which agglomeration becomes relevant is not determinable, but data suggest that the turning point is not only dependent on space holder volume fraction but also on space holder particle size.

The general effect of increased space holder volume fraction on creating higher pore connectivity [49] is easily observed using the μCT data. The role of pore connectivity in implantation and healing success has been considered in many recent publications on bone ingrowth into porous materials. These studies have led to the consensus that pore connectivity is crucial for osseointegration, as it allows more body fluids to be transported through pores [4, 12, 27]. This accelerates the healing process by allowing tissue to grow inside scaffolds and improve fixation [51]. The orientation of pores is another relevant

parameter for orthopedic scaffolds. Frequently mentioned is the relationship between pore orientation and mechanical properties of the scaffold [1, 5]. But also the less frequently mentioned dependency of permeability, and thus the flow of body fluids, on pore orientation is important [52]. Due to space holder particles being rectangular and SHM using uniaxial compaction during fabrication, all space holder particles have a tendency to move towards a plane perpendicular to the applied compaction pressure, schematically shown in Figure 4.1. As confirmed by μCT data, up to 70% of the pores are angled $\leq$30° from the horizontal plane. This corresponds with the observations of Cabezas-Villa et al. [39]. This obviously has a pronounced effect on the mechanical behaviour of the scaffold, which becomes anisotropic [37, 46, 53]. Research on anisotropy of scaffolds and the effect on absorption and bone ingrowth is inconclusive [27, 51].

4.3. Porosity characteristics

Based on the results of Archimedes' test and the porosity measurements of μCT, it can be concluded that there is a linear relationship between porosity and space holder volume fraction [50, 54]. However, both measurements show porosities lower than the mixed volume fractions of space holder particles. Arifvianto et al. [49] used coarse urea space holder particles and points out that the lower strength and stiffness of space holding particles compared to metal matrix powder led to a porosity reduction of approximately 10% after compaction. Čapek et al. [21] added to this theory by stating that that an increased compacting pressure on metal matrix powder reduced the micro porosity and thus the overall porosity. Thickening of struts and decrease of micro porosity during sintering decreased the final porosity a few percent more [32, 49, 55]. This phenomena should be more pronounced at fine [50] and rectangular [46] space holder particles, which is mainly observed in sample 2F and in the general lower measured porosity compared to the mixed space holder volume fraction. Samples in this study were fabricated at a constant, relatively high compaction pressure which resulted in a lower measured porosity than mixed volume fraction and caused further deviations at higher volume fractions of urea. Meaning that an increased space holder volume fraction leads to an relatively increased compactability and therefore relatively lower porosity.

4.4. Mechanical performance

In this research diametral compression was used to evaluate mechanical properties of iron scaffolds with a low height-to-diameter ratio. Uniaxial compression is a more common way of determining the mechanical properties of iron scaffolds [11, 32, 34]; although diametral compression values are converted to uniaxial compression values by means of a formula, comparison with other studies is only an approximation. During compression, bending of scaffold struts is considered to be the deformative mechanism in the elastic region. During the first phase of plastic deformation, stress concentrations cause collapsing of micro pores [42]. Stress concentrations at micro pores also initiate the first fracture points and failure of a scaffold. Another stress concentration was found by Čapek et al. [21] and Zhang et al. [48] when they used angular space holder particles. They reported that spherical macro pores significantly enhanced mechanical properties compared to the use of angular space holding particles. The use of angular space holder particles may have decreased the overall mechanical properties of the scaffolds in this study. However, no significant difference was found between coarse and fine space holders. The change in volume fraction, however, did show a significant trend. Similar to Arifvianto [42] and Jones et al. [27], who found a linear relationship between porosity and elastic modulus, Lee et al. [56] even suggested that porosity plays a key role in the elastic modulus of a scaffold, regardless of size or morphology of the space holders. These reports are corresponding with the findings in this study. With the 0.2% strain offset method, yield strength values were determined and comparable with those of iron scaffolds reported by Su et al. [32]. To prevent bone re-absorption, stiffness of a scaffold should be similar to that of bone [26, 57]. According to CES EduPack 2017 a human femur has an elastic modulus and compressive yield strength of 5.85-20.4 GPa and 0.581-208 MPa (depending on cortical or cancellous bone, man or woman, age, etc.), respectively. Therefore, iron scaffolds prepared in this study need to be stiffer and stronger before being applicable in bone tissue engineering.

4.5. Electrochemical performance

Based on PDP measurements, all iron samples showed similar values of corrosion current density. Since corrosion current density is normalized for the contact area of all samples, this clearly shows that all samples have the same corrosion mechanism. It is well known that micro structural features such as texture and dislocation density may affect the corrosion rate [58]. Particularly relevant here is the grain size, that is proportional to the grain boundary area, which is expected to be more chemically active during corrosion [59]. It can therefore be assumed that, differences in corrosion between samples, were not a result of unintended differences in grain size, but were purely a result of differences in pore structure.

4.6. Corrosion performance

There are still no standards available to measure the corrosion rate of iron scaffolds, but the weight loss measurement after immersion is the most widely applied method [19]. Following ASTM G31-72 standard a test duration of 11 days was suggested for iron immersion. An extra measurement point after 3 days was added to comprehend the characterization of the corrosion process. During immersion the pH of m-SBF was measured to be approximately 7.5. Between pH 4 to 10, the corrosion rate of iron is independent of the pH of the solution [60]. Li et al. [19] found that struts in the center of an additively manufactured scaffold (80% porosity) almost stayed intact. Furthermore, Jones et al. [27] mention that a throat radius of >50 μm was required to maintain high enough permeability, for vascularization and mineralization to occur in a porous implant. Both researchers emphasize the importance of permeability in absorption of scaffolds. Scaffolds used in this study have a long internal pore network with a lot of small, blocking throats. Therefore, permeability might be low and causing m-SBF to corrode iron mainly from the exterior of scaffolds. This belief is supported by μCT scans of scaffolds after immersion, which showed minimal pore volume or pore area differences in the internal structure, compared to μCT data before immersion. The low permeability is probably the main reason for minimal weight loss after immersion. Another reason for the low weight loss measured, or even the increase in weight, may be related to limitations of the weight loss measurement and sample cleaning [19]. For solid samples, weight loss measurement works quite well, because it is feasible to remove all corrosion products with minimum attack to the sample itself. In the case of highly porous scaffolds, however, it is difficult to remove all corrosion products. Especially for the center of scaffolds, an acid is needed for cleaning. However, this acid also removes iron from the scaffold itself. Visual inspection, SEM and EDS analysis suggest that after cleaning there are still remaining corrosion products, which might lead to a measured weight increase. Based on the reasoning above, it is difficult to compare corrosion data with other reports, since there are too many factors that could influence the results. When comparing mass loss measurements of this study, a significant difference between the different space holder volume fractions was found. A higher porosity means a higher corrosion rate. The small significant difference between 6C-11d and 6F-11d is specifically interesting and probably caused by the relatively lower area to volume ratio of 6F-11d who is, in combination with the high volume fraction, causing larger pore throats and a higher permeability. This theory is schematically represented in Figure 4.1 and corresponds with the ideas of Li et al. [19].

The effect of the corrosion on mechanical properties of the samples was studied after cleaning. However, as mentioned above, corrosion is minimal and therefore the effect on mechanical properties is minimal. Furthermore, SEM and EDS analysis suggest that after cleaning corrosion products remain on the scaffold, which might influence diametral compression measurements. Changes in the stiffness of an immersion-tested scaffold can be attributed to reduction in strut thickness and accumulation of corrosion products [19]. Changes in the strength of an immersion-tested scaffold can mainly be attributed to the strength of the remaining iron struts and the ability of the corrosion products to partly carry the load [19]. Since the strength of the scaffolds slightly decreases with increasing immersion time, corrosion products do not seem to carry any load while iron struts become thinner. Simultaneously, it is observed that the stiffness of the scaffolds remains the same for an increasing immersion time. This could mean that, although struts lose their thickness and thus the scaffold its stiffness, accumulating corrosion products antagonize this effect. However, the differences in measured results are small and a longer immersion time with larger pores would be advised for more divergent measurements. Furthermore, standardization for corrosion measurement of porous scaffolds would be advised.

4.7. Statistical analysis

In order to use the one-way ANOVA for statistical analysis the following assumptions were made; measurements for each group are independent, random and normally distributed. Furthermore, a conservative rule for using the one-way ANOVA is the homogeneity of the standard deviation between groups. Since the one-way ANOVA is considered a robust test, violations to this rule are tolerated rather well [61]. Therefore, the one-way ANOVA was used despite the observed variation in standard deviation between groups. To lessen the risk of an incorrect statistical analysis in future research, an increased number of samples per group should be used. This reduces the heterogeneity of the standard deviation between different groups.

5

Conclusions

An optimum porous design for orthopedic scaffolds is said to have macro pore sizes of approximately 100 to 400 μm, micro pores smaller than 20 μm and an open, interconnected structure. Within these specifications the sizes and shape of the pores, as well as the porosity of the scaffold, can still be varied to meet the requirements in mechanical properties and absorption rate. In this study space holder particle size and space holder volume fraction were studied to clarify the effects on the geometric characteristics and performance of absorbable iron scaffolds. With iron as the spherical matrix powder and urea as the rectangular space holder powder, six different scaffolds, with space holder volume fractions of 20%, 40% and 60% and space holder sizes of 408.5 μm and 248.6 μm, were successfully fabricated using the space holder method.

The space holder particle size directly affected the created pore size and surface area yet also changed the pore connectivity. Similarly, the space holder volume fraction directly affected the created porosity and pore connectivity yet also changed the pore size and shape. It can be concluded that the pore structure does not independently change due to space holder particle size or volume fraction, but rather as a combined effect of both. Furthermore, the rectangular shape of space holder particles and uniaxial compaction during fabrication induced inclinations of pores oriented perpendicular to compaction pressure, concluding that the space holder particle shape also influences the scaffold performance.

Furthermore, it can be concluded that the mechanical properties of a scaffold decrease with increasing space holder volume fraction. Space holder particle size did not affect the mechanical properties significantly. During 3 and 11 days immersion in m-SBF, the yield strength of the scaffolds decreased minimally while the elastic modulus remained the same.

Change in space holder size and volume fraction showed no effects on the corrosion mechanism of scaffolds. The differences in weight loss measurements are therefore a result of different pore structures. It can be concluded that weight loss of scaffolds due to corrosion increases for and increasing volume fraction of space holder particles. The effect of space holder particle size on weight loss was less pronounced and results suggested that the corrosion of porous iron scaffolds not only depends on surface area but also on pore throat size and the resulting permeability of a scaffold.

Altogether, this study demonstrated the effect of space holder usage on iron scaffolds for orthopedic applications.

6

Recommendations

The effects of space holder particle size and volume fraction on the pore structure, resultant mechanical properties and absorbability of iron scaffolds have been synthesized through surface, topological, corrosion and mechanical characterization. Changing the volume fraction of space holder particles in iron scaffolds clearly affected its corrosion and mechanical properties, but the effect of the size of space holder particles was less evident. Therefore, future studies should consider to:

1. Increase the size deviation of space holder particles. Results have shown that the corrosion and mechanical differences of iron scaffolds, created with space holder particles of D_{50}=408.5 μm and D_{50}=248.6 μm, are not significant. Optimal pores for orthopedic scaffolds are said to be approximately between 100 to 400 μm [27–30]. Hence, a larger contrast can be made.

2. Increase the space holder volume fraction. With the current SHM parameters, maximum measured porosity was 54%, however, Čapek et al. [21] was capable of creating a porosity of 82.3% with SHM. Adding a higher space holder volume fraction to iron provides more information on the correlation between fraction and its effect.

3. Use spherical space holder particles. Rectangular space holder particles caused unintended anisotropy, stress concentrations in sharp pore edges and small pore throats. Using spherical space holder particles might lead to stronger, isotropic scaffolds and higher corrosion rates caused by wider throats, leading to more optimal scaffolds for orthopedic use.

4. Measure weight loss of scaffolds after longer immersion time, allowing the effect of immersion to be more pronounced.

5. Measure permeability and throat size of scaffolds. Results have shown that the corrosion rate of a porous scaffold not only rely on surface area, but might also depend on throat size and permeability.

6. Use cold isostatic pressing at scaffold fabrication. This technique applies a uniform pressure at the die surface and can be used for creating large height-to-diameter shapes [62]. Hence, fabricated scaffolds are suitable for uniaxial compression tests and unintended anisotropy in the scaffold is prevented.

7. General; a standard to measure the corrosion of porous metallic scaffolds and a conclusive guideline on the mechanical and absorption demands of orthopedic scaffolds.

Acknowledgements

I would first like to thank my supervisor Dr. Jie Zhou, who was interested in the personal side of a story, whose door was always open when I needed guidance and who had the patience to let me work independently at my own pace. Throughout my thesis, I had a lot of support of Niko Putra, who I enjoyed working with both for his project as for mine. Likewise support was given to me by Sander Leeflang, Yageng Li and Teunis van Manen, who helped me in laboratory usage and who were always in for a friendly conversation or substantive discussion.

I would also like to acknowledge Arjan Mol and Balakrishnan Munirathinam for their discussions on corrosion and their help in electrochemical testing. Furthermore, I would like to acknowledge Michel van den Brink for helping me with laser diffraction measurements. A special thanks to Arjan Thijssen, who conducted the μCT scans and whose enthusiastic conversations helped relieve the scanning time. Lastly, I would like to thank Budi Arifvianto, whose doctoral research was really useful, both for physical as for mental resources.

Sybren de Vries
Delft, June 2019

Bibliography

[1] Wu, S., Liu, X., Yeung, K.W., Liu, C., Yang, X.: Biomimetic porous scaffolds for bone tissue engineering. Materials Science and Engineering: R: Reports 80, 1–36 (2014). doi: 10.1016/J.MSER.2014.04.001

[2] Blank, A.T., Riesgo, A.M., Gitelis, S., Rapp, T.B.: Bone grafts, substitutes, and augments in benign orthopaedic conditions: current concepts. Bulletin of the NYU Hospital for Joint Diseases 75(2), 119–128 (2017)

[3] Lichte, P., Pape, H.C., Pufe, T., Kobbe, P., Fischer, H.: Scaffolds for bone healing: Concepts, materials and evidence. Injury 42(6), 569–573 (2011). doi: 10.1016/j.injury.2011.03.033

[4] Zivic, F., Affatato, S., Trajanovic, M., Schnabelrauch, M., Grujovic, N.: Biomaterials in Clinical Practice : Advances in Clinical Research and Medical Devices. Springer International Publishing (2018)

[5] Ryan, G., Pandit, A., Apatsidis, D.P.: Fabrication methods of porous metals for use in orthopaedic applications. Biomaterials 27(13), 2651–2670 (2006). doi: 10.1016/j.biomaterials.2005.12.002

[6] Zheng, Y., Gu, X., Witte, F.: Biodegradable metals. Materials Science and Engineering: R: Reports 77, 1–34 (2014). doi: 10.1016/J.MSER.2014.01.001

[7] Bose, S., Roy, M., Bandyopadhyay, A.: Recent advances in bone tissue engineering scaffolds. Trends in Biotechnology 30(10), 546–554 (2012). doi: 10.1016/j.tibtech.2012.07.005

[8] Witte, F., Hort, N., Vogt, C., Cohen, S., Kainer, K.U., Willumeit, R., Feyerabend, F.: Degradable biomaterials based on magnesium corrosion. Current Opinion in Solid State and Materials Science 12(5-6), 63–72 (2008). doi: 10.1016/j.cossms.2009.04.001

[9] Schinhammer, M., Hänzi, A.C., Löffler, J.F., Uggowitzer, P.J.: Design strategy for biodegradable Fe-based alloys for medical applications. Acta Biomaterialia 6(5), 1705–1713 (2010). doi: 10.1016/j.actbio.2009.07.039

[10] He, J., He, F.L., Li, D.W., Liu, Y.L., Liu, Y.Y., Ye, Y.J., Yin, D.C.: Advances in Fe-based biodegradable metallic materials. RSC Advances 6(114), 112819–112838 (2016). doi: 10.1039/C6RA20594A

[11] Hermawan, H., Purnama, A., Dube, D., Couet, J.: Updates on the research and development of absorbable metals for biomedical applications. Progress in Biomaterials pp. 1–18 (2018). doi: 10.1007/s40204-018-0091-4

[12] Alvarez, K., Nakajima, H.: Metallic scaffolds for bone regeneration. Materials 2(3), 790–832 (2009). doi: 10.3390/ma2030790

[13] Vries de, S.: Synthesis of absorbable metal scaffolds for bone regeneration. Delft University of Technology (2018)

[14] Yu, W., Zhao, H., Ding, Z., Zhang, Z., Sun, B., Shen, J., Chen, S., Zhang, B., Yang, K., Liu, M., Chen, D., He, Y.: In vitro and in vivo evaluation of MgF 2 coated AZ31 magnesium alloy porous scaffolds for bone regeneration. Colloids and Surfaces B: Biointerfaces 149, 330–340 (2017). doi: 10.1016/j.colsurfb.2016.10.037

[15] Pogorielov, M., Husak, E., Solodivnik, A., Zhdanov, S.: Magnesium-based biodegradable alloys: Degradation, application, and alloying elements. Interventional Medicine and Applied Science 9(1), 27–38 (2017). doi: 10.1556/1646.9.2017.1.04

[16] Katarivas Levy, G., Ventura, Y., Goldman, J., Vago, R., Aghion, E.: Cytotoxic characteristics of biodegradable EW10X04 Mg alloy after Nd coating and subsequent heat treatment. Materials Science and Engineering C 62, 752–761 (2016). doi: 10.1016/j.msec.2016.01.086

[17] Liu, W., Wang, J., Jiang, G., Guo, J., Li, Q., Li, B., Wang, Q., Cheng, M., He, G., Zhang, X.: The Improvement of Corrosion Resistance Biocompatibility and Osteogenesis of the Novel Porous Mg-Nd-Zn Alloy. Journal of Materials Chemistry B 5(36), 7661–7674 (2017). doi: 10.1039/C7TB00920H

[18] Vojtěch, D., Kubásek, J., Čapek, J., Pospíšilová, I.: Comparative mechanical and corrosion studies on magnesium, zinc and iron alloys as biodegradable metals. Materiali in Tehnologije 49(6), 877–882 (2015). doi: 10.17222/mit.2014.129

[19] Li, Y., Zhou, J., Pavanram, P., Leeflang, M., Fockaert, L., Pouran, B., Tümer, N., Schröder, K.U., Mol, J., Weinans, H., Jahr, H., Zadpoor, A.: Additively manufactured biodegradable porous magnesium. Acta Biomaterialia 67, 378–392 (2018). doi: 10.1016/J.ACTBIO.2017.12.008

[20] Gong, H., Wang, K., Strich, R., Zhou, J.G.: In vitro biodegradation behavior, mechanical properties, and cytotoxicity of biodegradable Zn-Mg alloy. Journal of Biomedical Materials Research Part B: Applied Biomaterials 103(8), 1632–1640 (2015). doi: 10.1002/jbm.b.33341

[21] Čapek, J., Vojtěch, D., Oborná, A.: Microstructural and mechanical properties of biodegradable iron foam prepared by powder metallurgy. Materials and Design 83, 468–482 (2015). doi: 10.1016/j.matdes.2015.06.022

[22] Hermawan, H., Purnama, A., Dube, D., Couet, J.: Fe–Mn alloys for metallic biodegradable stents: Degradation and cell viability studies. Acta Biomaterialia 6(5), 1852–1860 (2010). doi: 10.1016/J.ACTBIO.2009.11.025

[23] Wegener, B., Sievers, B., Utzschneider, S., Müller, P., Jansson, V., Rößler, S., Nies, B., Stephani, G., Kieback, B., Quadbeck, P.: Microstructure, cytotoxicity and corrosion of powder-metallurgical iron alloys for biodegradable bone replacement materials. Materials Science and Engineering: B 176(20), 1789–1796 (2011). doi: 10.1016/J.MSEB.2011.04.017

[24] Quadbeck, P., Hauser, R.: Iron based cellular metals for degradable synthetic bone replacement. PM2010 World Congress (2010). doi: 10.1017/CBO9781107415324.004

[25] Peuster, M., Hesse, C., Schloo, T., Fink, C., Beerbaum, P., von Schnakenburg, C.: Long-term biocompatibility of a corrodible peripheral iron stent in the porcine descending aorta. Biomaterials 27(28), 4955–4962 (2006). doi: 10.1016/J.BIOMATERIALS.2006.05.029

[26] Lewis, G.: Properties of open-cell porous metals and alloys for orthopaedic applications. Journal of Materials Science: Materials in Medicine 24(10), 2293–2325 (2013). doi: 10.1007/s10856-013-4998-y

[27] Jones, A.C., Arns, C.H., Hutmacher, D.W., Milthorpe, B.K., Sheppard, A.P., Knackstedt, M.A.: The correlation of pore morphology, interconnectivity and physical properties of 3D ceramic scaffolds with bone ingrowth. Biomaterials 30(7), 1440–1451 (2009). doi: 10.1016/J.BIOMATERIALS.2008.10.056

[28] Murphy, C.M., Haugh, M.G., O'Brien, F.J.: The effect of mean pore size on cell attachment, proliferation and migration in collagen-glycosaminoglycan scaffolds for bone tissue engineering. Biomaterials 31(3), 461–466 (2010). doi: 10.1016/j.biomaterials.2009.09.063

[29] Van Bael, S., Chai, Y., Truscello, S., Moesen, M., Kerckhofs, G., Van Oosterwyck, H., Kruth, J.P., Schrooten, J.: The effect of pore geometry on the in vitro biological behavior of human periosteum-derived cells seeded on selective laser-melted Ti6Al4V bone scaffolds. Acta Biomaterialia 8(7), 2824–2834 (2012). doi: 10.1016/j.actbio.2012.04.001

[30] Yuan, H., Kurashina, K., De Bruijn, J.D., Li, Y., De Groot, K., Zhang, X.: A preliminary study on osteoinduction of two kinds of calcium phosphate ceramics. Biomaterials 20(19), 1799–1806 (1999). doi: 10.1016/S0142-9612(99)00075-7

[31] Chou, D.T., Wells, D., Hong, D., Lee, B., Kuhn, H., Kumta, P.N.: Novel processing of iron-manganese alloy-based biomaterials by inkjet 3-D printing. Acta Biomaterialia 9(10), 8593–8603 (2013). doi: 10.1016/j.actbio.2013.04.016

[32] Su, M., Wang, H., Chen, C.: Effects of Micropores on Processing and Properties of Porous Irons. Applied Mechanics and Materials 863, 26–32 (2017). doi: 10.4028/www.scientific.net/AMM.863.26

[33] Alavi, R., Trenggono, A., Champagne, S., Hermawan, H.: Investigation on Mechanical Behavior of Biodegradable Iron Foams under Different Compression Test Conditions. Metals 7(12), 202 (2017). doi: 10.3390/met7060202

[34] Čapek, J., Msallamová, ., Jablonská, E., Lipov, J., Vojtěch, D.: A novel high-strength and highly corrosive biodegradable Fe-Pd alloy: Structural, mechanical and in vitro corrosion and cytotoxicity study. Materials Science and Engineering: C 79, 550–562 (2017). doi: 10.1016/J.MSEC.2017.05.100

[35] Yang, C., Huan, Z., Wang, X., Wu, C., Chang, J.: 3D Printed Fe Scaffolds with HA Nanocoating for Bone Regeneration. ACS Biomaterials Science and Engineering 4(2), 608–616 (2018). doi: 10.1021/acsbiomaterials.7b00885

[36] Arifvianto, B., Zhou, J.: Fabrication of metallic biomedical scaffolds with the space holder method: A review. Materials 7(5), 3588–3622 (2014). doi: 10.3390/ma7053588

[37] Banhart, J.: Manufacture, characterisation and application of cellular metals and metal foams. Progress in Materials Science 46(6), 559–632 (2001). doi: 10.1016/S0079-6425(00)00002-5

[38] Schindelin, J., Arganda-Carreras, I., Frise, E., Kaynig, V., Longair, M., Pietzsch, T., Preibisch, S., Rueden, C., Saalfeld, S., Schmid, B., Tinevez, J.Y., White, D.J., Hartenstein, V., Eliceiri, K., Tomancak, P., Cardona, A.: Fiji: an open-source platform for biological-image analysis. Nature Methods 9(7), 676–682 (2012). doi: 10.1038/nmeth.2019

[39] Cabezas-Villa, J.L., Olmos, L., Bouvard, D., Lemus-Ruiz, J., Jiménez, O.: Processing and properties of highly porous Ti6Al4V mimicking human bones. Journal of Materials Research pp. 1–12 (2018). doi: 10.1557/jmr.2018.35

[40] Jones, J.R., Poologasundarampillai, G., Atwood, R.C., Bernard, D., Lee, P.D.: Non-destructive quantitative 3D analysis for the optimisation of tissue scaffolds. Biomaterials 28(7), 1404–1413 (2007). doi: 10.1016/J.BIOMATERIALS.2006.11.014

[41] Sahasrabudhe, S.N., Rodriguez-Martinez, V., O'Meara, M., Farkas, B.E.: Density, viscosity, and surface tension of five vegetable oils at elevated temperatures: Measurement and modeling. International Journal of Food Properties pp. 1–17 (2017). doi: 10.1080/10942912.2017.1360905

[42] Arifvianto, B.: Synthesis and Evaluation of Porous Titanium Scaffolds Prepared with the Space Holder Method for Bone Tissue Engineering (2017)

[43] Oyane, A., Kim, H.M., Furuya, T., Kokubo, T., Miyazaki, T., Nakamura, T.: Preparation and assessment of revised simulated body fluids. Journal of Biomedical Materials Research 65A(2), 188–195 (2003). doi: 10.1002/jbm.a.10482

[44] Md Saad, A.P., Jasmawati, N., Harun, M.N., Abdul Kadir, M.R., Nur, H., Hermawan, H., Syahrom, A.: Dynamic degradation of porous magnesium under a simulated environment of human cancellous bone. Corrosion Science 112, 495–506 (2016). doi: 10.1016/j.corsci.2016.08.017

[45] McCafferty, E.: Validation of corrosion rates measured by the Tafel extrapolation method. Corrosion Science 47(12), 3202–3215 (2005). doi: 10.1016/J.CORSCI.2005.05.046

[46] Bekoz, N., Oktay, E.: Effects of carbamide shape and content on processing and properties of steel foams. Journal of Materials Processing Technology 212(10), 2109–2116 (2012). doi: 10.1016/j.jmatprotec.2012.05.015

[47] Bafti, H., Habibolahzadeh, A.: Production of aluminum foam by spherical carbamide space holder technique-processing parameters. Materials and Design 31(9), 4122–4129 (2010). doi: 10.1016/j.matdes.2010.04.038

[48] Zhang, J., Wu, L., Jing, D., Ding, J.: A comparative study of porous scaffolds with cubic and spherical macropores. Polymer 46(13), 4979–4985 (2005). doi: 10.1016/j.polymer.2005.02.120

[49] Arifvianto, B., Leeflang, M., Zhou, J.: Characterization of the porous structures of the green body and sintered biomedical titanium scaffolds with micro-computed tomography. Materials Characterization 121, 48–60 (2016). doi: 10.1016/J.MATCHAR.2016.09.026

[50] Tuncer, N., Arslan, G., Maire, E., Salvo, L.: Investigation of spacer size effect on architecture and mechanical properties of porous titanium. Materials Science and Engineering A 530(1), 633–642 (2011). doi: 10.1016/j.msea.2011.10.036

[51] Fiedler, T., Belova, I.V., Murch, G.E., Poologasundarampillai, G., Jones, J.R., Roether, J.A., Boccaccini, A.R.: A comparative study of oxygen diffusion in tissue engineering scaffolds. Journal of Materials Science: Materials in Medicine 25(11), 2573–2578 (2014). doi: 10.1007/s10856-014-5264-7

[52] Ho, S.T., Hutmacher, D.W.: A comparison of micro CT with other techniques used in the characterization of scaffolds. Biomaterials 27(8), 1362–1376 (2006). doi: 10.1016/j.biomaterials.2005.08.035

[53] Kim, S.W., Jung, H.D., Kang, M.H., Kim, H.E., Koh, Y.H., Estrin, Y.: Fabrication of porous titanium scaffold with controlled porous structure and net-shape using magnesium as spacer. Materials Science & Engineering C 33, 2808–2815 (2013). doi: 10.1016/j.msec.2013.03.011

[54] Jian, X., Hao, C., Guibao, Q., Yang, Y., Xuewei, L.: Investigation on relationship between porosity and spacer content of titanium foams. Materials & Design 88, 132–137 (2015). doi: 10.1016/J.MATDES.2015.08.125

[55] Laptev, A., Bram, M., Buchkremer, H.P., Stöver, D.: Study of production route for titanium parts combining very high porosity and complex shape. Powder Metallurgy 47(1), 85–92 (2004). doi: 10.1179/003258904225015536

[56] Lee, B., Lee, T., Lee, Y., Lee, D.J., Jeong, J., Yuh, J., Oh, S.H., Kim, H.S., Lee, C.S.: Space-holder effect on designing pore structure and determining mechanical properties in porous titanium. Materials & Design 57, 712–718 (2014). doi: 10.1016/j.matdes.2013.12.078

[57] Čapek, J., Vojtěch, D.: Microstructural and mechanical characteristics of porous iron prepared by powder metallurgy. Materials Science and Engineering: C 43, 494–501 (2014). doi: 10.1016/j.msec.2014.06.046

[58] Obayi, C.S., Tolouei, R., Paternoster, C., Turgeon, S., Okorie, B.A., Obikwelu, D.O., Cassar, G., Buhagiar, J., Mantovani, D.: Influence of cross-rolling on the micro-texture and biodegradation of pure iron as biodegradable material for medical implants. Acta Biomaterialia 17, 68–77 (2015). doi: 10.1016/j.actbio.2015.01.024

[59] Ralston, K.D., Birbilis, N.: Effect of Grain Size on Corrosion: A Review. CORROSION 66(7), 075005–075005 (2010). doi: 10.5006/1.3462912

[60] DOE. Fundamentals handbook chemistry. Volume 1 of 2. Tech. rep. (1993)

[61] Baldi, B., Moore, D.S.: The practice of statistics in the life sciences (2014)

[62] Thümmler, F., Oberacker, R.: An introduction to powder metallurgy. Institute of Materials (1993)

[63] Bakan, H.I.: A novel water leaching and sintering process for manufacturing highly porous stainless steel. Scripta Materialia 55(2), 203–206 (2006). doi: 10.1016/j.scriptamat.2006.03.039

[64] Lei, C., Wang, Q., Li, L.: Effect of interactions between poly(vinyl alcohol) and urea on the water solubility of poly(vinyl alcohol). Journal of Applied Polymer Science 114(1), 517–523 (2009). doi: 10.1002/app.30504

[65] Feng, Y., Gaztelumendi, N., Fornell, J., Zhang, H., Solsona, P., Baró, M., Suriñach, S., Ibáñez, E., Barrios, L., Pellicer, E., Nogués, C., Sort, J.: Mechanical properties, corrosion performance and cell viability studies on newly developed porous Fe-Mn-Si-Pd alloys. Journal of Alloys and Compounds 724, 1046–1056 (2017). doi: 10.1016/J.JALLCOM.2017.07.112

[66] O'Keefe, R.J., Jacobs, J.J., Chu, C.R., Einhorn, T.A., American Academy of Orthopaedic Surgeons.: Orthopaedic Basic Science : Foundations of Clinical Practice. American Academy of Orthopaedic Surgeons (2013)

[67] Bram, M., Stiller, C., Buchkremer, H.P., Stöver, D., Baur, H.: High-Porosity Titanium, Stainless Steel, and Superalloy Parts. Advanced Engineering Materials 2(4), 196–199 (2000). doi: 10.1002/(SICI)1527-2648(200004)2:4<196::AID-ADEM196>3.0.CO;2-K

[68] Özkan, N., Briscoe, B.J.: Characterization of die-pressed green compacts. Journal of the European Ceramic Society 17(96), 697–711 (1997). doi: 10.1016/S0955-2219(96)00090-8

[69] Yang, W.W., Yang, K.Y., Wang, M.C., Hon, M.H.: Solvent debinding mechanism for alumina injection molded compacts with water-soluble binders. Ceramics International 29(7), 745–756 (2003). doi: 10.1016/S0272-8842(02)00226-2

[70] Arifvianto, B., Leeflang, M.A., Zhou, J.: A new technique for the characterization of the water leaching behavior of space holding particles in the preparation of biomedical titanium scaffolds. Materials Letters 120, 204–207 (2014). doi: 10.1016/j.matlet.2014.01.087

[71] Jain, H., Gupta, G., Kumar, R., Mondal, D.: Microstructure and compressive deformation behavior of SS foam made through evaporation of urea as space holder. Materials Chemistry and Physics 223, 737–744 (2019). doi: 10.1016/J.MATCHEMPHYS.2018.11.040

[72] German, R.M., Bose, A.: Injection Molding of Metals and Ceramics. Metal Powder Industries Federation (1997)

A

Appendix - Fabrication of scaffolds

This section is created during the process of finding the right combinations of parameters used in SHM during fabrication of porous iron scaffolds. It is only meant as a guide for creating iron samples using the space holder method.

Mixing Addition of a binder was needed to prevent segregation of iron and urea. Segregation is the separation of mixed powder components both due to differences in density and size. With a binder added to the mixture, granular materials are formed, composed of space holding particles, coated with smaller metal matrix particles [36, 46, 63]. Poly vinyl alcohol (PVA) was chosen as the binder in this study. PVA to water weight percentages were tested between 0% and 14%, which was tested in binder solution to iron volume percentages between 1.5% and 6%, see Figure A.1. Unfortunately, it turned out that urea and PVA react with each other during mixing [64], making the binder solution less effective. However, using pure demineralized water as binder still caused segregation after mixing and no other binder was at hands. The best results were achieved using a high-concentration low-volume PVA solution, which was mixed with iron to create a small film of binder around matrix powder particles.

Rectangular urea (fine D_{50}=248.6 μm and coarse D_{50}=408.5 μm) to spherical iron (D_{90}=60.83 μm) volume percentages were tested in a range between 0% and 80%, of which 60% was the highest achievable porosity, given the current tools [42].

In combination with iron as the metal matrix powder ammonium bicarbonate [21], natrium chloride [65] and corn starch [32] have been used as space holder for iron scaffolds, where only Čapek et al. [21] used a binder (hexane) during mixing. Although Feng et al. [65] does not mention segregation, Su et al. [32] specifically picked a space holder size similar to the iron size in order to achieve a uniform distribution of pores. However, pore sizes between 100 and 400 μm have said to be optimal for orthopedic scaffolds [13, 66] and it has been reported that matrix particles should be several times smaller than space holding particles in order to improve the sinterability of metal matrix powder [67].

Compaction A single uniaxial compaction press was used up to its maximum pressure of 5 metric tons (resulting in 370 MPa). Compaction time was tested at 2, 5 and 10 minutes, of which 5 minutes is used in this study, see Figure A.1. The die was filled with the same volume of mixture every time, creating green compacts of roughly 4 mm high or a height-to-diameter ratio of 0.3. This low height-to-diameter ratio was chosen specifically to keep a uniform compaction pressure throughout the scaffold which results therefore in uniform density [42]. The highest compacting pressure from uniaxial pressing was experienced by powder particles located at the circumference near the punch and the lowest compacting pressure was found near the circumference of the lower part of the compact [62, 68], which became more pronounced at an increasing height-to-diameter ratio [36]. A low height-to-diameter ratio provides an even distribution of green density and strength, which prevents collapsing of areas with lower green density during space holder removal. Čapek et al. [21] needed a pressure of 1020 MPa to compact cylindrical samples a ratio of 4.0; specifically the green compact with smaller iron powder (2-80 μm) was more prone to collapsing compared to the green compact with larger iron powder (10-200 μm). Using a fine powder will cause interparticle bridging and increase the friction during compaction, therefore, under the same conditions fine powder will be less compacted than coarse powder [36, 62].

Drying After compaction drying the green compacts at 110°C for 60 minutes was tried to remove remaining water from the binder solution in order to increase strength of the binder. An increased strength might be useful during leaching, where the removal of urea and maybe even dissolving of PVA might cause collapsing of the green compact. However, no positive effects on the leaching outcome were found, see Figure A.1. Therefore, the only drying of the fabricated scaffolds was at room temperature during fabrication time (ft).

Leaching Space holders in the green compact can be removed by heating the green compact, causing space holder particles to evaporate. Another option is by submerging the green compact in a liquid, causing space holder particles to dissolve (leaching). Leaching the green compact with water is preferred because water is non-toxic and non-flammable. Furthermore, the use of water as a leaching agent eliminates environmental drawbacks related to the removal of organic space holders and does not involve the anisotropic thermal expansion associated with typical organic substances [63]. As an additional benefit, equipment necessary for water leaching is very simple. Increasing the temperature of water increases the efficiency of the process [69]. Removal rate of the space holder decreases as leaching time increases due to the increased length of porous channels, through which space holders must travel to diffuse [63]. Immersing the green compact in water does not remove all space holder particles because not all particles, and thus pores, are interconnected. To measure the removal of space holder particles during leaching Arifvianto et al. [70] developed a high accuracy weight measurement technique. In a follow-up study Arifvianto and Zhou [36] found that only about 69% of the total urea particles could be removed from a scaffold if the scaffold had 50.5 vol% space holder fraction. Effectiveness of leaching increases if the space holder fraction is higher. Considering the fact that removal of space holder can also be done by decomposing urea at high temperatures [71], meaning that both sintering and dwelling help urea removal; the fact that Arifvianto and Zhou [36] found, that maximum urea removal by leaching of 60% porous titanium scaffolds took place after roughly 15 minutes; the fact that after testing from 2 till 30 minutes of leaching, 20 minutes was found as the maximum time for the green compacts to keep their original shape, see Figure A.1. Urea removal is performed by leaching in demineralized water for 20 minutes.

Dwelling Since the vaporization point of urea is around 150 °C [71] dwelling the brown compacts (after leaching) was tried for 4 hours at both 190 °C and 250 °C to remove the remaining urea before sintering [21, 32]. However, no positive effects compared to regular sintering were found, see Figure A.1. Since dwelling increased fabrication time by 4 hours, it is not used in this study.

Sintering Sintering is a high temperature treatment process that causes powder particles to bond to each other with only minor changes to particle shape [5]. Sintering at high temperatures leads to neck formation and neck growth; this leads to the densification of the structure and improvement of structural integrity [5]. Necking is related to metallurgical bonding between powder particles [36]. A small oxide layer covering powder particles can prevent this bonding, however increasing compaction pressure may break up the oxide film and create metallurgical bonding between powder particles, increasing sinterability [37]. Laptev et al. [55] reported that, after sintering a scaffold created by the space holder method, shrinkage of the scaffold mainly occurred due to reduction in size of micro pores but that the macro pores usually retained their sizes. The number of micro pores decreases when the sintering temperature is increased [32]. Cabezas-Villa et al. [39] and Lee et al. [56] found that the sintered metal matrix was less dense when volume fraction of space holders increased, which suggests that sintering is perturbed by the presence of more pores. Exposure to atmospheric air during the sintering process may lead to contamination of scaffolds and deteriorate the mechanical properties [36]. To prevent contamination a furnace can be made to work under vacuum or an inert gas can be flushed into the sintering furnace. The optimum sintering temperature and time are found by trial and error and can be checked after sintering by a compression test, observation of interparticle neck growth or by performing a microstructural analysis [36]. In this study sintering was tested at 1000 °C and 1200 °C for both 4 hours, of which 1200 °C showed more necking and higher strength. As shown by German and Bose [72], the heating rate during sintering is just as important as the final temperature, you can save time by increasing the heating rate but this can cause slumping, defects and cracks. A ramp rate of 1, 2 and 10 °C/minute were tested, of which a heating rate 10 °C/minute showed slumping, see Figure A.1. In this study a furnace flushed with Argon gas, a ramp rate of 2 °C/minute, set point of 1200 °C, 4 hours of sintering and natural cooling, were used.

Mixing						Compaction		Drying		Leaching	Results	Dwelling		Sintering			Results
Binder (PVA)		Time	Urea		Time	Pressure	Time	Time	Temperatu	Time	Leaching	Time	Temperatu	Ramp rate	Set point	Time	Sintering
Weight % t	Volume %	Minutes	Size um	Volume %	Minutes	Mpa	Minutes	Minutes	Celcius	Minutes	Pass	Minutes	Celcius	C/min	Celcius	Hours	Pass
			0	0	0	370	10	ft	20	30	V						
		0	400	80	60	370	5	ft	20	5	X						
							2	ft	20	10	V			2	1000	4	!
0	0	30	400	60	30	370	10	ft	20	20	V			2	1200	4	V
							2	ft	20	10	V			2	1000	4	X
	1.5	30	400	60	30	370	10	ft	20	20	V			2	1200	4	!
					30	370	2	ft	20	10	!						
						110	5	ft	20	10	X						
						185	5	ft	20	10	!						
						260	5	ft	20	10	!						
				60	150	370	5	ft	20	10	!						
				70	150	370	5	ft	20	10	X						
				75	150	370	5	ft	20	10	X						
						110	5	ft	20	10	X						
						185	5	ft	20	10	X						
						260	5	ft	20	10	X						
		30	400	80	150	370	5	ft	20	10	X						
														1	1000	4	X
										0				10	1000	4	V
										25	V						
				20	180	370	2	ft	20	30	V						
												240	190	10			X
										0				10	1000	4	!
										2	V			2	1000	4	V
										25	V						
				40	180	370	2	ft	20	30	!						
												240	190	10			X
										0				1	1000	4	X
										2	V			2	1000	4	!
										25	V						
			200	60	180	370	2	ft	20	30	!						
												240	250	10	1000	4	V
										0				10	1000	4	V
										10	V	240	250	10	1000	4	V
										25	V						
				20	180	370	2	ft	20	30	V						
												240	190	10			X
										0				1	1000	4	X
										2	V			2	1000	4	V
				40	180	370	2	ft	20	30	!						
				50	180	370	10	ft	20	20	!						
													190	10			X
												240	250	10	1000	4	X
														1	1000	4	X
										0				10	1000	4	X
										2	V			2	1000	4	X
										10	V	240	250	10	1000	4	X
				60	180	370	2	ft	20	30	X						
				70	180	370	10	ft	20	15	X						
	3	60	400	80	60	370	10	ft	20	10	X						
		30	400	60	150	370	5	ft	20	10	X						
	6	60	400	80	60	370	10	ft	20	10	X						
	9	30	400	60	150	370	5	ft	20	10	X						
				50	60	370	5	ft	20	10	X						
6	10	60	400	70	60	370	5	ft	20	10	X						
				20	60	370	5	ft	20	20	V			2	1200	4	V
				40	60	370	5	ft	20	20	V			2	1200	4	V
			200	60	60	370	5	ft	20	20	!			2	1200	4	V
				20	60	370	5	ft	20	20	V			2	1200	4	V
				40	60	370	5	ft	20	20	V			2	1200	4	V
							2	ft	20	10	V			2	1000	4	V
					30	370	10	ft	20	20	V			2	1200	4	V
	1.5	30	400	60	60	370	5	ft	20	20	V			2	1200	4	V
								90	40	20	!						
							2	ft	20	10	V			2	1000	4	V
	3	30	400	60	30	370	10	ft	20	20	V						
	14	30	400	60	30	370	2	ft	20	10	X						
10	24	30	400	60	30	370	2	ft	20	10	X						
								60	110	20	V			2	1200	4	V
	1.5	30	400	60	30	370	2	ft	20	10	!						
								60	110	20	!						
	3	30	400	60	30	370	2	ft	20	10	X						
	11	30	400	60	30	370	2	ft	20	10	X						
	18	30	400	60	30	370	2	ft	20	10	X						
14	24	30	400	60	30	370	2	ft	20	10	X						

Figure A.1: This flow diagram is created during the process of finding the right combination of parameters used in SHM during fabrication of porous iron scaffolds. Values are only meant as a guide for creating iron samples using the space holder method. Results consist of passing (V), barely passing (!) and failing (X) visual inspection, both for leaching and sintering.
The samples with 10wt.% PVA to water, 1.5vol.% solution to iron and 5 minutes compaction are used during this study.

B

Appendix - Supplementary data

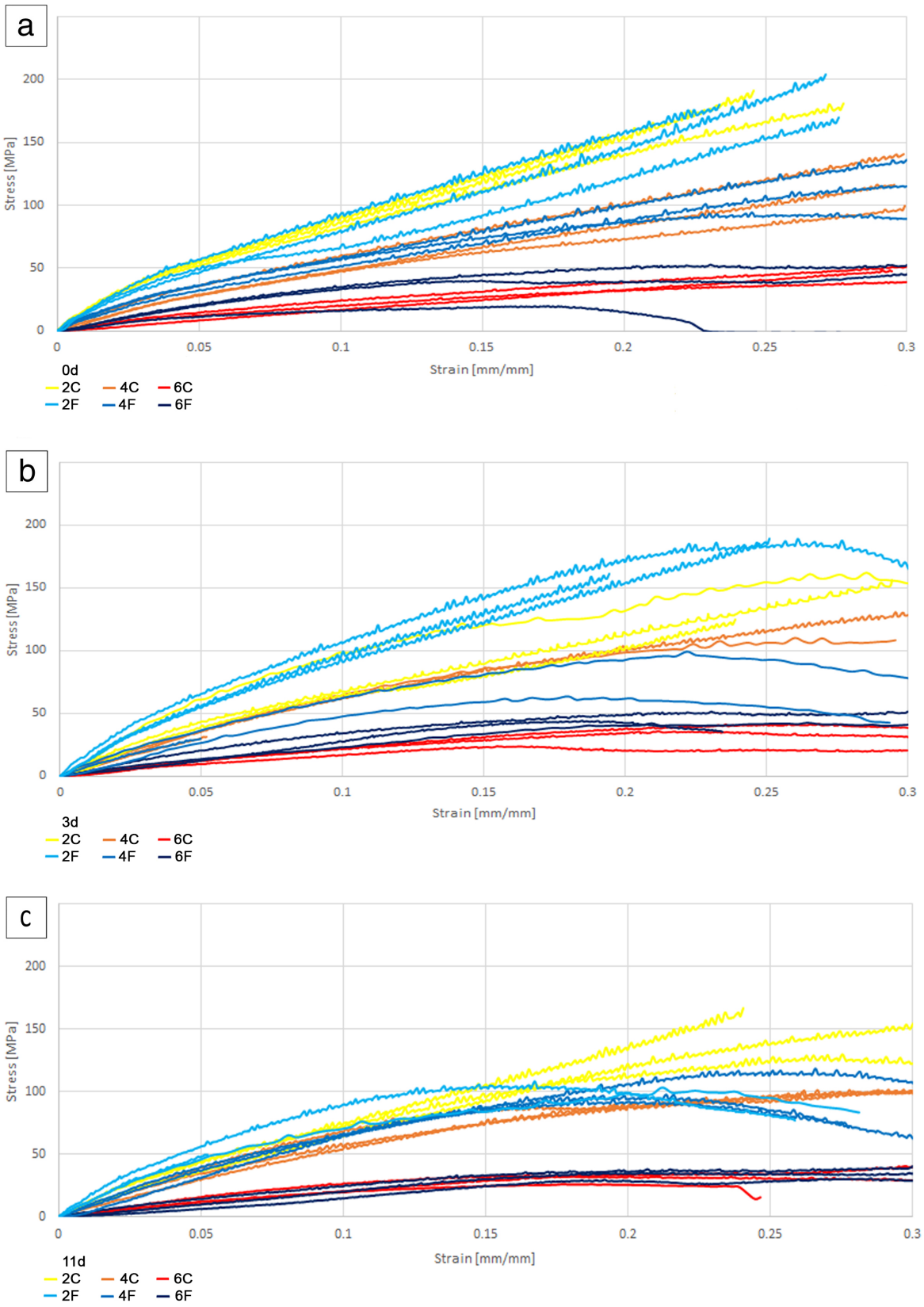

Figure B.1: Stress strain curves of every sample, by diametral compression, three samples per configuration. a: before immersion, b: after 3 days immersion, c: after 11 days immersion

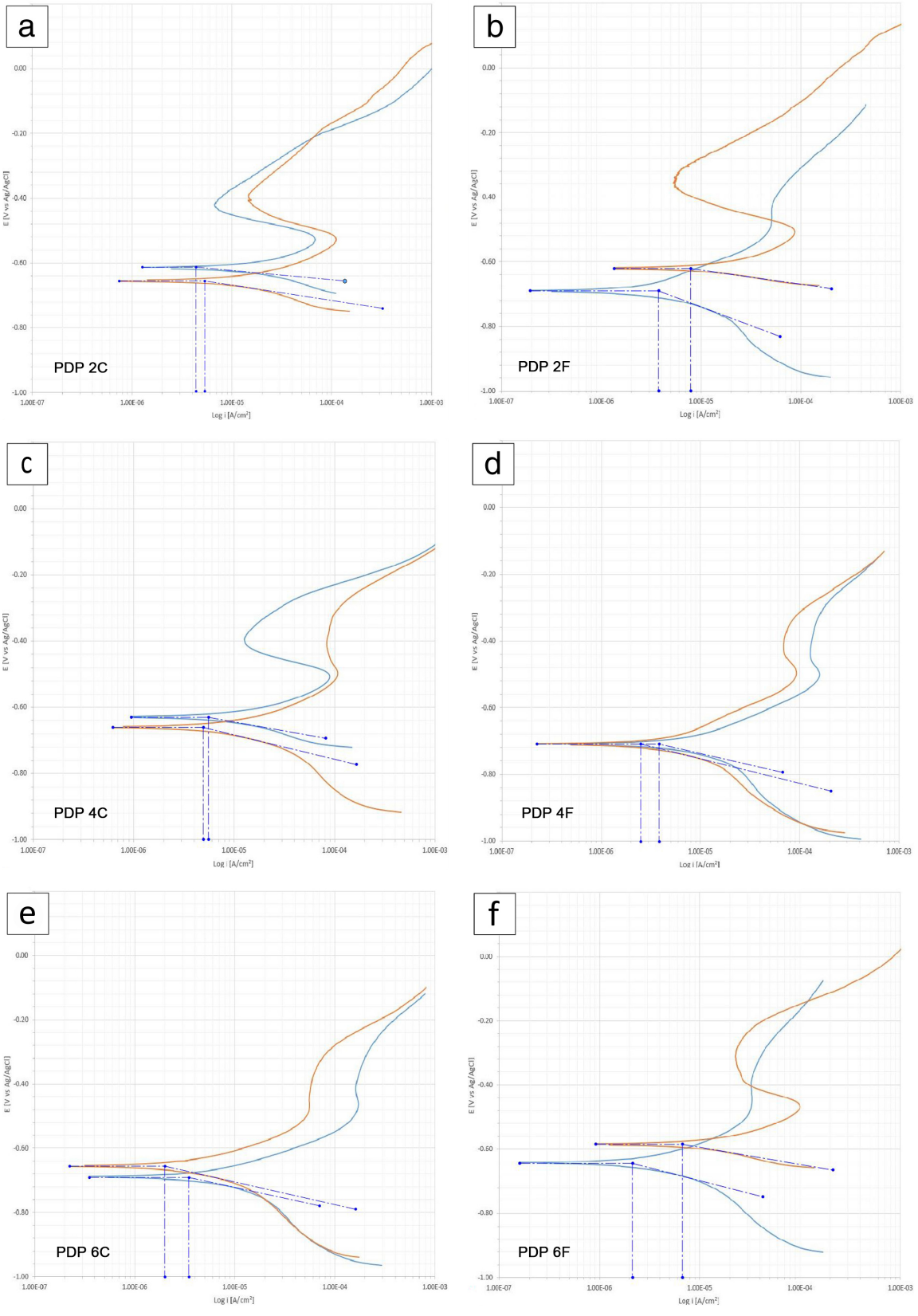

Figure B.2: PDP curves of every sample, including Tafel extrapolation, two samples per configuration. a: 2C, b: 2F, c: 4C, d: 4F, e: 6C, f: 6F